





Dynamics and apparent permeability of the glycocalyx layer: Start-up and pulsating shear experiments *in silico*

Vlasis Mitsoulas , Stylianos Varchanis , Yannis Dimakopoulos ,* and John Tsamopoulos 
*Laboratory of Fluid Mechanics and Rheology, Department of Chemical Engineering,
University of Patras, Greece*



(Received 6 August 2020; accepted 22 December 2021; published 14 January 2022)

The response of the endothelial glycocalyx (EG) to variations of the hemodynamic environment is of vital importance for the regulation of the blood vessel permeability and the balance of the blood components. Thus, it is necessary to quantify fundamental properties such as its apparent permeability, in addition to dynamic quantities like drag and torque on EG nanofibers, which are indicators of the glycocalyx mechanical integrity, and determine their dependence on the individual geometric features and mechanical properties of a single fiber. Because of the $O(100\text{ nm})$ height of the fibers and the lack of relevant technology, these would be difficult to determine experimentally. In the present study, we model the flow of blood plasma over and past the EGL as a 3D dynamic viscous flow over and past an array of deformable fibers. We perform *in silico* start-up and pulsating shear experiments that typically appear in vessels of different sizes of the circulatory system in a representative volume of the fibrous glycocalyx layer. Numerical as well as analytical predictions for the tip displacement vector under steady-state conditions show that the horizontal and vertical components scale linearly and quadratically with the inverse blockage ratio, respectively. The dimensionless apparent permeability and the spatial-average velocity in the EG layer follow the same scalings as the vertical tip displacement. In the start-up shear flow, the fiber elasticity is found to contribute only to the transient phase, not to the steady value of the dimensionless apparent permeability, which is determined exclusively by the geometric ratios of the matrix. In the pulsatile flow only, backflow develops with the thickness of the order of the fiber radius and introduces asymmetries in the forward and the backward evolution of important quantities. Moreover, and for small ratios of the elastic to viscous forces, the time-average apparent EGL permeability is larger by at least an order of magnitude from the Darcy permeability for rigid EGL fibers. This finding gives an alternative perspective to the efficiency of paracellular and transcellular transport processes of biological molecules, plasma ions, and viruses.

DOI: [10.1103/PhysRevFluids.7.013102](https://doi.org/10.1103/PhysRevFluids.7.013102)

I. INTRODUCTION

The fibrous layer covering the luminal surface of the vascular endothelium is called endothelial glycocalyx layer (EGL) [1]. Research on it has been increasing since it has been associated with multiple biological processes in microcirculation. Functions such as angiogenesis [2,3], cancer metastasis [4], haemostasis [5], fluid and solute exchange [6], coagulation [7], and inflammatory responses [8] depend on phenomena occurring close to the endothelial surface. Many experimental studies [9,10] demonstrate the existence of this hairy-like pericellular network attached to the surface of the endothelium, which is mainly composed of membrane-bound glycoprotein and

*Corresponding author: dimako@chemeng.upatras.gr; <http://fluidslab.chemeng.upatras.gr/>

glycolipid chains [1,11,12]. Over the past decades, insight has been gained into the role of the EG, which has been identified to be the main mechanosensor and mechanotransducer of blood shear-stress on endothelial cells [13–15]. It also acts as a molecular filter that limits access of circulating blood plasma constituents to the endothelial cell membrane and the intercellular space between neighboring endothelial cells [16–20] affecting paracellular and transcellular transport processes (e.g., drug delivery or entry of viruses), since it controls the capillary permeability [21].

In an effort to improve the understanding of the role of the glycocalyx in biochemical processes, some studies systematically investigated and finally identified the sophisticated geometrical pattern of the fibers on the surface of endothelial cells. Specifically, Squire *et al.* [22] proposed a geometrical model representing the EG as a quasiperiodic arrangement. This model was later advanced by Weinbaum *et al.* [13] into an ideal periodic bush-structure with distinct spatial characteristics. In theoretical hemodynamics, where the effective medium theory has been used to model blood plasma flow in the porous EGL, the findings of Squire *et al.* [22] proved significant and constituted the basis of all subsequent efforts to evaluate the EGL's hydrodynamic properties such as its permeability, i.e., the capability of EGL to allow fluid transmission [23].

Pioneering in the determination of the normal to the flow permeability constant (k_{pm}) are the general studies of Kuwabara [24], Hasimoto [25], and Sangani and Acrivos [26], who reported solutions for flows past randomly and equidistantly distributed impermeable solids of spherical and cylindrical shape. Specifically, the last authors presented numerical solutions for the slow flow perpendicular to square and hexagonal periodic arrays of cylinders and managed to analytically express the dimensionless drag force in terms of the volume fraction c of the cylinders. Their conclusions were adopted by several authors [27–36] and were associated with the evaluation of k_{pm} of the layer consisting of a fibrous network. However, these studies were performed under the assumption that the fibers maintain their initial position and cylindrical shape during the flow development and exert a time-independent drag force, which diverges from the actual biological process of blood flows in microvessels, where transient hemodynamic and structural phenomena arise. Thus, critical issues associated with the motion of the glycoproteins and their effect on EGL apparent permeability cannot be addressed and remain unanswered. Indicatively, two major open questions related to these issues are: Does the motion of the EG because of fiber flexibility play a crucial role in determining the apparent permeability of the EGL when the latter is treated as a porous medium? If so, what is the effect of the EGL elasticity on the apparent permeability? Answering these questions is the motivation for the present work.

In general, there are limited theoretical studies that consider the elastic response of EGL irrespective of the determination of its permeability or not. Damiano *et al.* [37] treated the EGL as a deformable layer implementing a biphasic mixture model to describe the poro-elastohydrodynamics of the layer. The elastic behavior of the EGL was also examined by Vink, Duling, and Spaan [38]. They measured the transient restoration of the EGL after it was almost entirely compressed by the passage of a white blood cell in a tightly fitting capillary, finding that the characteristic time for this restoration is approximately 0.4 s. Damiano and Stace [39], Weinbaum *et al.* [13], and Han *et al.* [40] attempted to predict this characteristic time using an electrochemical mechanism, linear elastic theory, and large-deformation theory, respectively, to describe the recoil of the crushed EGL. Even though in a way, these macroscopic approaches incorporate the EGL's elasticity, the motion of the fibers is neglected in the determination of the permeability. Such an assumption has been made in nearly all recent theoretical studies [41–43] for the blood plasma flow in EGL. Apart from continuum methods, recent studies employed fully atomistic molecular dynamics simulations to reveal the glycocalyx dynamics. An all-atom glycocalyx model with detailed composition was first introduced by Cruz-Chu *et al.* [44]. They studied its response to shear flow and its property to act as a sieve for fibroblast growth factors, which are associated with functions such as angiogenesis and wound healing. Despite their revealing results regarding the dynamics of the system, the flow regime was characterized by velocity fields of magnitude significantly higher than the ones developed in real physiology. Constructing a similar flow/glycocalyx molecular system, Jiang

et al. [45] investigated the dynamics of the flow driven by physiologically relevant forces and outlined shear stress distributions in varying glycocalyx configurations. These studies considered EG's complicated structure, composition, and flexibility and shed light on events inside the layer, enriching the understanding of glycocalyx-related diseases. However, there is a need to seek an alternative mesoscopic method that can accurately predict such composite structural-hydrodynamic phenomena with a smaller computational cost.

From a fluid mechanical perspective, the EGL/blood plasma system belongs to the category of flows over "hairy surfaces" [36,46,47]. Soft, porous beds made of deformable filamentous fibers which are permeated by viscous fluids are commonly encountered in nature [36,46,48], including coral reefs and submerged aquatic canopies [49,50], rain forest canopies [51], and have been studied both for their biological [52,53] and industrial [54–58] importance. Despite the broadness of the category and the relatively large number of excellent theoretical contributions, no attempts have been made to answer the open questions mentioned above. This is related to the lack of appropriate stable numerical algorithms for handling the 3D spatial variations in response to or in conjunction with the flow fluctuations.

In the present study, we account for the elasticity of EG and its spatial complexity (hexagonal periodic array of cylinders [13]) to address the open issues mentioned above for the first time. Through a microscopic 3D simulation employing a mixed finite element method (FEM), we investigate in detail the interaction between blood plasma and the glycocalyx solid structure to predict the dynamic behavior of the coupled system, e.g., stress, pressure, and velocity fields, and how it affects the EGL apparent permeability. Specifically, we examine start-up and pulsating shear experiments characterized by variations in the fiber elastic modulus (E_f) and the fiber-to-fiber distance (D), to acquire information about the dependency of the apparent permeability and other characteristic variables on such properties. Finally, the predictions of the DNS simulator are compared with those of an analytical model at steady-state flow conditions based on the linear deflection theory and the assumption of slow flow in a porous medium (Appendix B).

II. PROBLEM FORMULATION

It has been documented that red blood cell (RBC) aggregation at low-shear rates and excluded volume effects lead to compaction of the central cell core, thus forming a core-region rich in RBCs and a cell-depleted marginal sleeve of suspending fluid (plasma) at the periphery of the vessel [1,59] also known as cell-free-layer (CFL) [60]. Adopting this hemodynamical process of RBCs migration in a microvessel of radius $R_{\text{vessel}} = 20 \mu\text{m}$ [Fig. 1(a)], we consider the 3D incompressible plasma flow perpendicular to the fibrous network in the EG attached on the vascular wall [Fig. 1(b)].

A. Theoretical modeling of the process

The physical domain consists of two subdomains representing the solid (elastic fibers) and fluid (blood plasma) phases [Fig. 1(b)], the complexity of which emerges from the sophisticated structure of the EG hairy network. The glycocalyx fibers are modeled as deformable, hyperelastic cylindrical rods with density ρ_f and Young's modulus E_f , anchored vertically to the endothelium of the vessel. The subscripts p and f denote the blood plasma and EG fiber phases, respectively. We do not consider any interactions (e.g., nematic, Van der Waals forces, etc.) among them except those induced by the flow. Since there is evidence that the proteinic clusters that form EG exhibit a hexagonal spatial periodicity [22], we assume that the fibers follow the idealized pattern proposed by Weinbaum *et al.* [13], and shown in Fig. 2(a). Both experimental [61] and theoretical studies [62] have concluded that blood plasma exhibits non-negligible viscoelastic properties; however, in the present study, we will consider blood plasma as a Newtonian fluid with density ρ_p and dynamic viscosity η_p . This simplification originates from the fact that the gyroscopic radius of the proteins

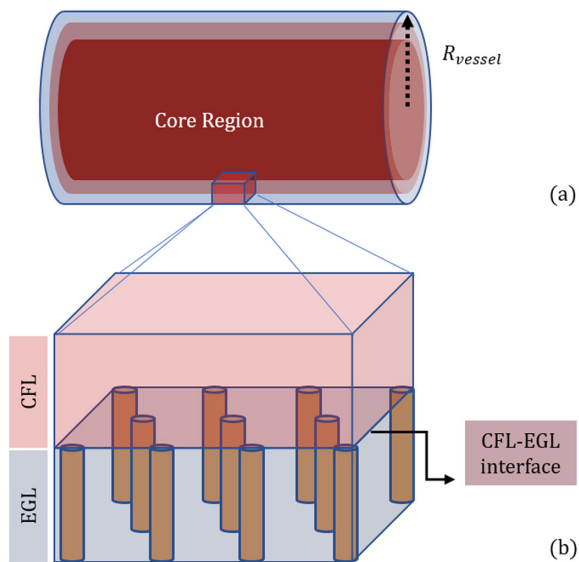


FIG. 1. (a) A representation of the vessel lumen and its RBC-rich core region. (b) The region of the vessel that is under investigation and a representation of the EGL and CFL. The cylinders inside the EGL represent the fibers, while the remaining space is occupied by blood plasma.

that attribute elasticity to blood plasma [62] are of the same order of magnitude as the glycocalyx fibers and their relative distance. Thus, in the length scale that we examine, the response of the solvent is necessarily viscous. Finally, the curvature of the EGL is neglected due to the small ratio of the height of the glycocalyx fibers to the radius of the vessel [$O(0.01)$].

We define the connecting straight line between two adjacent fibers as the x -coordinate, and we assume that the angle of attack (AoA) of blood flow is zero with respect to it. Due to the hexagonal distribution of the fibers, our formulation holds for every $AoA = n\pi/3$, where $n = 0, 1, 2, \dots$. Estimated values for the fiber radius R_f , and fiber-to-fiber distance D can be found in the literature [22,13] to be approximately 5–6 nm and 20–30 nm, respectively. Even though the instantaneous fiber vertical height $h(t)$ retains a physiological scaling, its value presents variations primarily associated with the blood vessel type and size and the organism the EG belongs to. Squire *et al.* [22] reported that a typical value of h_o in a frog mesenteric microvessel is 50–100 nm reaching up to 300–400 nm in the case of inflamed vessels. Marsh and Waugh [63] suggested that the luminal layer thickness of human umbilical vein endothelial cells (HUVECs) is about 380 nm, and generally, a qualitative agreement in measurements of h_o can be found in several studies [13,64–66] indicating that EG can be up to 500 nm in height. In the present paper, we consider $R_f = 5$ nm, $D = 20$ –30 nm, and the initial undeformed fiber height $h_o = 150$ nm; these values are close to those of EG of HUVECs.

Furthermore, determining the computational domain representative of the entire structure and minimizing the computational cost proved to be quite challenging. The microscopic nature of our approach does not allow considering a large domain of many glycocalyx fibers. Instead, we identified an elementary periodic 3D space, which reflects the scale of the luminal layer. We develop a minimal spatial configuration [Figs. 2(a) and 2(b)], which is utilized in our analysis and can accurately represent the EGL through the concepts of symmetry and periodicity. The height of the blood plasma region, referring to the CFL thickness L is of the order of 1 μm in microvessels [67,68]. In this study, we set $L = 820$ nm. Then $L + h_o$ is the location of the upper boundary of the physical domain.

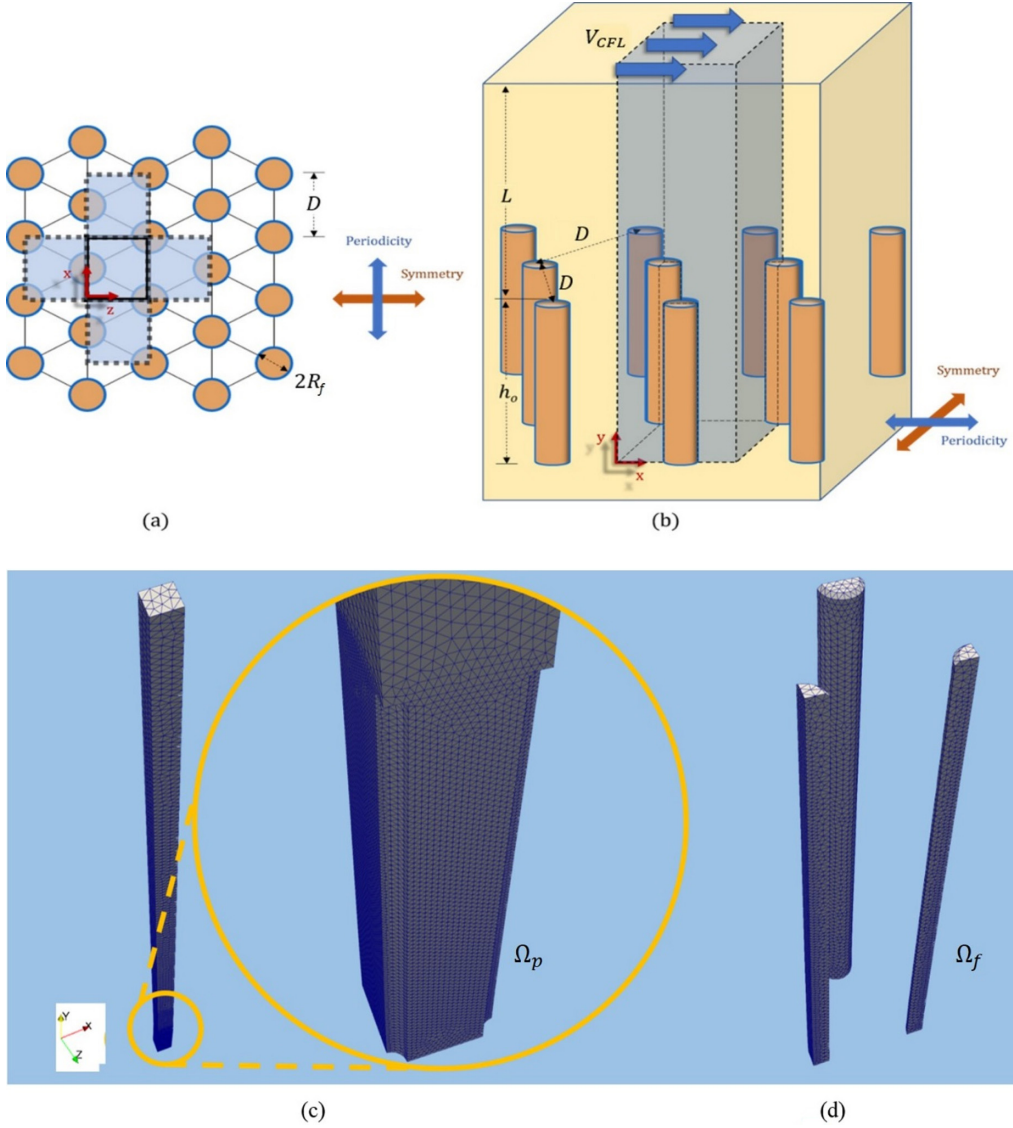


FIG. 2. (a) Top view of the periodic hexagonal structure of EG. A graphical representation from [13,22]. The minimal elementary domain is represented by the solid, black-lined rectangle, which follows vertical periodicity (in the x -direction) and horizontal symmetry (in the z -direction). (b) Side view of the 3D periodic structure with undeformed fiber height equal to h_0 [$= h(t = 0)$], (c) the finite element tessellated plasma domain, and (d) the finite-element tessellated fibrous domain.

B. Governing equations

We scale all lengths with the fiber radius R_f , velocities with the velocity of the core V_{CFL} , and times with the characteristic flow time R_f/V_{CFL} . In addition, both the pressure and stress components are scaled with a viscous scale, $\eta_p V_{CFL}/R_f$. The dimensionless groups that arise are the Reynolds number, $Re = \rho_p V_{CFL} R_f / \eta_p$, the density ratio, $d_R = \rho_f / \rho_p$, the ratio of the elastic to viscous forces, $H_K = E_f R_f / (\eta_p V_{CFL})$, the aspect ratio of the fiber $A_R = h_0 / R$, and the blockage ratio

$B_R = 2R_f/D$, which takes values between 0 and 1. The governing equations for each subdomain, in their dimensionless form, are presented below.

The blood plasma dynamics are governed by the momentum balance [Eq. (1)] and continuity equation [Eq. (2)]

$$\text{Re} \left(\frac{\partial \underline{u}_p}{\partial t} + (\underline{u}_p - \underline{w}_p) \cdot \underline{\nabla} \underline{u}_p \right) = \underline{\nabla} \cdot \underline{\underline{\sigma}}_p, \quad (1)$$

$$\underline{\nabla} \cdot \underline{u}_p = 0. \quad (2)$$

The Cauchy stress tensor $\underline{\underline{\sigma}}_p$ is given as $\underline{\underline{\sigma}}_p = -p_p \underline{I} + (\underline{\nabla} \underline{u}_p + \underline{\nabla} \underline{u}_p^T)$. Equation (1) is expressed in the arbitrary Lagrangian-Eulerian (ALE) formulation, in which the fluid domain is moving, requiring the introduction of the mesh velocity \underline{w}_p in the convective term [69–73]. In the fluid domain, this velocity is related to the displacement vector of the mesh nodes through the following expression:

$$\frac{\partial \underline{d}_p}{\partial t} = \underline{w}_p, \quad (3)$$

where \underline{d}_p is the displacement vector subjected to

$$\underline{\nabla}^2 \underline{d}_p = 0. \quad (4)$$

The glyocalyx structural dynamics is governed by the momentum balance [Eq. (5)], continuity equation [Eq. (6)], and the relation [Eq. (7)] for the isotropic part of the stress tensor p_f in the EG fibers:

$$\text{Re} \, d_R \frac{\partial \underline{u}_f}{\partial t} = \underline{\nabla} \cdot \underline{\underline{\Pi}}_f, \quad (5)$$

$$\det(\underline{F}) = 1, \quad (6)$$

$$p_f = \lambda(\text{tr} \underline{G}), \quad (7)$$

where \underline{u}_f is the local velocity of the fibers. Since solid kinematics follow the Lagrangian framework, \underline{u}_f is related to the mesh displacement vector \underline{d}_f and mesh velocity vector \underline{w}_f via the following expressions:

$$\frac{\partial \underline{d}_f}{\partial t} = \underline{u}_f, \quad (8)$$

$$\underline{w}_f = \underline{u}_f. \quad (9)$$

In this study, the fibers are considered to be hyperelastic solids following the Saint Venant–Kirchoff model, which is expressed via the second Piola-Kirchoff stress tensor as $\underline{\underline{S}}_f = p_f \underline{I} + 2\mu \underline{G}$, where λ and μ are the dimensionless Lamé constants, and $\underline{G} = \frac{1}{2}(\underline{F}^T \cdot \underline{F} - \underline{I})$ is the Green strain tensor. The first Piola-Kirchoff stress tensor $\underline{\underline{\Pi}}_f$ is related to $\underline{\underline{S}}_f$ by the expression $\underline{\underline{\Pi}}_f = \underline{F} \cdot \underline{\underline{S}}_f$ where $\underline{F} = \underline{I} + \underline{\nabla} \underline{d}_f$ is the deformation gradient tensor. Also, $\underline{\underline{\sigma}}_f = \det(\underline{F})^{-1} \underline{F} \cdot \underline{\underline{S}}_f \cdot \underline{F}^T$, where $\underline{\underline{\sigma}}_f$ is the Cauchy stress tensor. The dimensionless Lamé constants are related to solid mechanical properties of elasticity and compressibility through the expressions $\mu = \frac{H_K}{2(1+\nu)}$ and $\lambda = \frac{\nu H_K}{(1+\nu)(1-2\nu)}$, where ν is the Poisson ratio. The assumption that the fibers are hyperelastic solids has been made to allow for large displacements, which linear elastic models cannot account for. The Saint Venant–Kirchoff is a widely used hyperelastic stress-strain constitutive model suitable for computational

fluid-structure interaction formulations and proved to preserve stability when modeling structures with large displacements [74]. Moreover, it has only two parameters that can be determined easily.

C. Boundary conditions

The fluid-structure interaction between the plasma and the fibers comes with the imposition of the conditions on their interfacial boundary. There, we set a balance between forces from blood plasma and fiber sides [Eq. (10)], equality between the corresponding velocities [Eq. (11)], and finally, equality between the corresponding local grid velocities [Eq. (12)]:

$$\underline{\underline{\sigma}}_f \cdot \underline{n}_f = \underline{\underline{u}}_p \cdot \underline{n}_p, \quad (10)$$

$$\underline{\underline{u}}_f = \underline{\underline{u}}_p, \quad (11)$$

$$\underline{\underline{w}}_f = \underline{\underline{w}}_p, \quad (12)$$

where \underline{n}_f , \underline{n}_p are the outward unit normal vectors of the respective domains. On the interface between the CFL and the core region [top boundary, $y = A_R + L/R_f$, in Fig. 2(b)], the dimensionless velocity is assumed to be either unity or time-varying in the x -direction [Eq. (13)]:

$$\underline{\underline{u}}_p = u_p^{\text{top}} \underline{e}_x. \quad (13)$$

More details on u_p^{top} are given in the Results section.

On the surface of the immobile endothelial cells [bottom boundary, $y = 0$, in Fig. 2(b)], we impose the no-slip and no-penetration conditions for the velocity.

On the CFL-core region interface, as well as on the surface of endothelial cells, the mesh remains fixed [Eq. (14)]:

$$\underline{\underline{w}}_p = \underline{0}. \quad (14)$$

The front and back, $z = 0$, of the unit representative volume [Fig. 2(b)] are assumed symmetry planes, while at the left and right boundaries, $x = 0$, $2B_R$, [Fig. 2(b)] periodicity is applied.

D. Numerical method

The governing equations are spatially discretized using the mixed finite element method (FEM). For the solution of the fluid-structure interaction problem, we implement the fully monolithic coupling methodology with the global unknown vector being $\underline{X} = \{\underline{u}, p, \underline{w}\}$. The corresponding mixed element is the P2-P0-P1 element. The use of the P0 element is necessary to resolve the pressure discontinuity between the two phases. The fibrous and plasma domains are tessellated in tetrahedral meshes of elements, as shown in Figs. 2(c) and 2(d), respectively. The unstructured mesh of tetrahedral elements is generated using the Netgen algorithm [75]. In all simulations, except for the mesh convergence study, the basic Netgen parameters that we used are the following: Max element size = 1.8, Min element size = 0.4, and Fineness = moderate. Finally, for the time integration, we use the fully implicit Euler method with the timestep $dt = 10^{-2}$ and initial conditions $\underline{X}^0 = \{\underline{0}, 0, \underline{0}\}$. The usual tests have been performed to determine convergence of the results with mesh and timestep refinement (see Appendix A).

E. Fiber and blood plasma properties

The material properties used in our simulations are summarized in Table I. Their values are taken from the indicated papers. For simplicity, we consider that blood plasma density and dynamic viscosity are close to those of water [62]. On the other hand, the choice of EG's material and mechanical properties turned out to be rather challenging. Given that the backbone molecules of

TABLE I. Typical material properties.

Property	Symbol	Values used	Literature
Topology	–	Hexagonal	Hexagonal [13], quasihexagonal [22]
Fiber radius	R_f	5 nm	5–6 nm [13,22]
Velocity at the CFL/core interface	V_{CFL}	1 mm/s	0.1–10 mm/s [31]
Fiber spacing (between their centerlines)	D	15–35 nm	20 nm [13,22]
Initial fiber height	h_0	150 nm	150–400 nm [13], 50–100 nm [22] ~380 ± 50 nm [63] 118–878 nm [78]
Fiber Young modulus	E_f	1–100 kPa	0.7–1.2 kPa [63], 0.39 kPa [76]
Fiber Poisson ratio	ν	0.49	
Fiber density	ρ_f	1410 kg/m ³	1410 kg/m ³ [76]
Plasma density	ρ_p	1000 kg/m ³	1025 kg/m ³ [62]
Plasma dynamic viscosity	η_p	10 ⁻³ Pa s	1.95 × 10 ⁻³ Pa s [62]

the glycocalyx are proteoglycans and glycoproteins of high molecular weight, we assume that EG's density can be approximated by $\rho_f = 1410 \text{ kg/m}^3$ [76]. As already discussed, research on the mechanical properties of glycocalyx is quite limited; however, there have been reports that indicate that EG's Young modulus is of the order of 1 kPa [63,77,78]. All the aforementioned studies on the geometrical and mechanical properties of the glycocalyx are cornerstones to the present work for restricting the parameter values used within physiological margins. In addition to the parametric analysis regarding the spacing between adjacent fibers, we investigate the dynamics of glycocalyx characterized by Young's modulus with the reported order of magnitude and one to two orders higher, reaching the asymptotic state of undeformable rigid bodies. In Table II the derived dimensionless groups are summarized. Since $\text{Re} \ll 1$, inertia could be neglected from Eqs. (1) and (5). However, the time dependency of the model is associated with the ALE and Lagrangian description of the fluid and solid phases [Eqs. (3) and (8)], respectively.

III. CALCULATION OF MACROSCOPIC QUANTITIES

To quantify the effect of basic geometric parameters and material properties such as the fiber-to-fiber distance and the fiber flexibility on the response of the glycocalyx, we calculate the apparent

TABLE II. Derived dimensionless groups.

Dimensionless number	Symbol	Definition	Value
Ratio of the elastic to viscous forces	H_K	$E_f R_f / (\eta_p V_{\text{CFL}})$	8.9–890
Reynolds	Re	$\rho_p V_{\text{CFL}} R_f / \eta_p$	$3.12 \times 10^{-6} \ll 1$
Aspect ratio	A_R	h_0 / R_f	30
Blockage ratio	B_R	$2R_f / D$	0.25–0.7
Density ratio	d_R	ρ_f / ρ_p	1.41

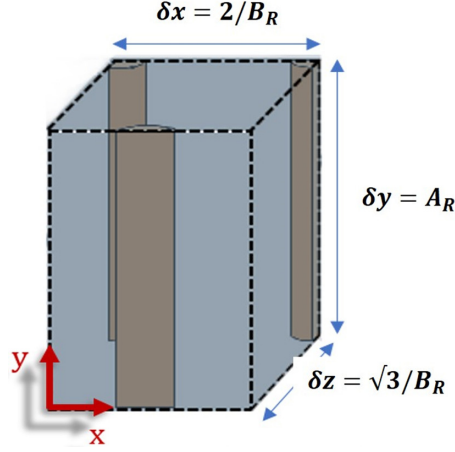


FIG. 3. Part of the physical domain, which corresponds to the porous layer and where fluid and solid phases coexist.

permeability of the porous medium formed by the glycocalyx layer, as well as the drag force and the torque exerted on a fiber.

A. Apparent permeability calculation

When the layer where the solid obstacles are present is treated as a porous medium (pm), the momentum balance is simplified to include the flow resistance resulting in the Brinkman equation, which for a creeping flow [79] and in dimensionless form is given by

$$0 = \nabla \cdot \underline{\underline{\sigma}} - \frac{1}{k_{pm}} \underline{\underline{u}}_{pm}, \quad (15)$$

where the term $-\frac{1}{k_{pm}} \underline{\underline{u}}_{pm}$ is the flow resistance, $k_{pm} = \frac{K}{R_f^2} \left(\frac{\eta_{pm}}{\eta_p} \right)$ is the dimensionless effective permeability, η_{pm} is the effective dynamic viscosity of the fluid in the porous medium, and K is the permeability constant. In our microscopic 3D simulations, the flow resistance that the EG exerts on plasma can be calculated after solving Eqs. (1)–(14) as a dimensionless drag force F_D :

$$F_D = \underline{\underline{F}}_t \cdot \underline{\underline{e}}_x = \left[\int (\underline{\underline{n}}_p \cdot \underline{\underline{\sigma}}_p) dS_{\text{int}} \right] \cdot \underline{\underline{e}}_x, \quad (16)$$

where S_{int} is the fluid-solid interface area, and $\underline{\underline{n}}_p$ the normal unit vector with respect to the fluid subdomain. In Eq. (15), $\underline{\underline{u}}_{pm}$ refers to the velocity vector inside a homogeneous apparent medium, which combines solid and fluid material properties. To find a representative velocity from the velocity field computed by the 3D fluid-solid interaction model, we compute the average velocity

$$\underline{\underline{U}} = \frac{\iiint_{\Omega_p} \underline{\underline{u}}_p dx dy dz + \iiint_{\Omega_f} \underline{\underline{u}}_f dx dy dz}{\iiint_{\Omega_p + \Omega_f} dx dy dz} \quad (17)$$

in a control volume, which encompasses the region of both fluid and solid (Fig. 3). In the above relationships, Ω_p and Ω_f are the fractions of the EGL occupied by the plasma and EG, respectively. Given that the front and back planes of the control volume are assumed symmetry planes, and the right and left boundaries are periodic, a mass balance at the control volume in Fig. 3 leads to the fact that $\underline{\underline{U}}$ is in the x -direction and can be expressed as $\underline{\underline{U}} = \bar{U} \underline{\underline{e}}_x$. Thus, we get a velocity vector that corresponds to a single-phase approximation of the glycocalyx-plasma system. Moreover, we approximate $\underline{\underline{u}}_{pm}$ by the average velocity of the domain $\underline{\underline{U}}$. The resisting force $\underline{\underline{F}}_R$ of the apparent

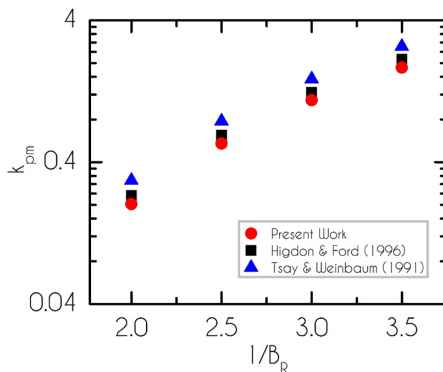


FIG. 4. A comparison between the steady apparent permeability calculated by Eq. (20) and those derived from the expressions in [27,28] for $\beta_R = 0.286, 0.33, 0.40,$ and 0.50 for rigid cylinders.

porous medium with permeability k_{pm} can now be calculated:

$$\underline{F}_R = \delta x \delta y \delta z \frac{\bar{U}}{k_{pm}} \equiv \frac{\underline{Q}}{k_{pm}}, \quad (18)$$

where $\underline{Q} = \delta x \delta y \delta z \bar{U}$ is the integral of the velocity calculated after solving Eqs. (1)–(14) over the 3D domain presented in Fig. 3.

If we equate the two forces under the action-reaction statement, $\underline{F}_R = -\underline{F}_t$, and using Eqs. (16)–(18), we can determine the apparent permeability constant:

$$k_{pm} = \frac{\|\underline{Q}\|}{\|\underline{F}_t\|}. \quad (19)$$

Similar to Eq. (19), correlations between drag force and permeability constant are commonly found in the literature [27,28,33], expressing the inverse proportionality of flow resistance and permeability [80]. However, in contrast to these relations, Eq. (19) emerges directly from the dynamics of the system and provides the way to explicitly determine the permeability in the case of interacting fluid-solid phases neglecting limitations regarding the shape, rigidity, orientation, and spatial distribution of the solid obstacles.

We compare our predictions with those suggested by Tsay and Weinbaum [27] and Hidgon and Ford [28] for the case of flow past a periodic hexagonal array of rigid cylinders for $\beta_R = 0.286, 0.33, 0.4,$ and 0.5 . Assuming $\frac{\eta_f}{\eta_p} \approx 1$, their analytical expressions for K in terms of k_{pm} are

$$k_{pm} = 0.0572 \left[2 \left(\frac{1}{B_R} - 1 \right) \right]^{2.377} \quad (20)$$

and

$$k_{pm} = \frac{\ln(c^{-0.5}) - 0.745 + c - \frac{c^2}{4}}{4c}, \quad (21)$$

respectively, where $c = \frac{\pi}{2\sqrt{3}} B_R^2$ is the volume fraction of fibers, having a maximum value equal to $c_m = \frac{\pi}{2\sqrt{3}}$. Our results are in very good agreement with those derived by Eqs. (20) and (21), as shown in Fig. 4, and reveal that Eq. (21) is closer to the DNS predictions.

B. Drag force and torque on a fiber

Another important feature in our analysis is the direct measurement of quantities such as the drag and torque that plasma flow exerts on a single EG fiber. Both quantities are useful for representing the fiber dynamics and are associated with the estimation of EGL relaxation time using elementary bending models [30,44]. Due to the nature of the computational domain represented as the elementary blue hexahedron in Fig. 2(b) that confines two quarters and a half of a fiber, or equivalently a complete fiber in total, Eq. (16) gives the drag force that a single fiber is subjected to. Such a force acts in the same direction as the plasma flow, namely here in the x -direction. To this end, to calculate the total torque on a single nanofiber with respect to its fixed base at $y = 0$, we need to find the coordinate y of the equivalent point load of the distributed force per unit area $\underline{n}_p \cdot \underline{\sigma}_p$ on S_{int} , which is given by

$$y_{\text{point}} = \frac{\int (\underline{n}_p \cdot \underline{\sigma}_p) \cdot \underline{e}_x y \, dS_{\text{int}}}{\int (\underline{n}_p \cdot \underline{\sigma}_p) \cdot \underline{e}_x \, dS_{\text{int}}}. \quad (22)$$

Then we can determine the total torque on a single EG fiber as

$$\underline{T}_D = (y_{\text{point}} \underline{e}_y) \times (F_D \underline{e}_x). \quad (23)$$

C. Space-averaged velocities inside the EGL

Essential definitions are also those of the space-averaged velocity of plasma (p) and the EG (f) inside the EGL. The corresponding space-averaged velocities $\bar{\underline{U}}_p$ and $\bar{\underline{U}}_f$ are given by Eqs. (24) and (25):

$$\bar{\underline{U}}_p = \frac{\iiint_{\Omega_p} \underline{u}_p \, dx dy dz}{\iiint_{\Omega_p} dx dy dz}, \quad (24)$$

$$\bar{\underline{U}}_f = \frac{\iiint_{\Omega_f} \underline{u}_f \, dx dy dz}{\iiint_{\Omega_f} dx dy dz} \quad (25)$$

IV. RESULTS

A. Start-up shear

1. Local dynamics and effect of blockage ratio

We begin our analysis by investigating the most common rheometric flow, the start-up shear [81]. To this end, we assume that the main bloodstream is steady. A typical value of the velocity at the CFL-core interface, V_{CFL} , in a microvessel of radius $R_{\text{vessel}} \in [10 \mu\text{m}, 40 \mu\text{m}]$ is of the order of 1 mm/s [82]. Here, we assume $V_{\text{CFL}} = 0.624$ mm/s. The corresponding dimensionless shear velocity in the x -direction, $u_p^{\text{top}} = 1$, is applied as a boundary condition [Eq. (13)] in the CFL-core interface. This provides information about the magnitude of the elastic effects compared to the viscous effects of a complex interacting system, and it is commonly used in *in vitro* rheometric experiments [83] and theoretical studies [35], and also is often assumed in the microcirculation [84,85].

Under these conditions, our results indicate a rapid increase in the deformation of the fibers at the beginning of the simulation, followed by an asymptotic steady state (see also the supplemental material, movie 1 [86]). The deformations are associated with the bending of the fiber body, which is increased in the proximity of the fixed base of the fiber producing a substantial change in its orientation. In Fig. 6(a) below one can see the fiber deformation with time along with the blood plasma streamlines. By defining the orientation angle θ as the angle between the fibers' initial and instantaneous normal directions of its top surface, we monitor the changing orientation of the fibers,

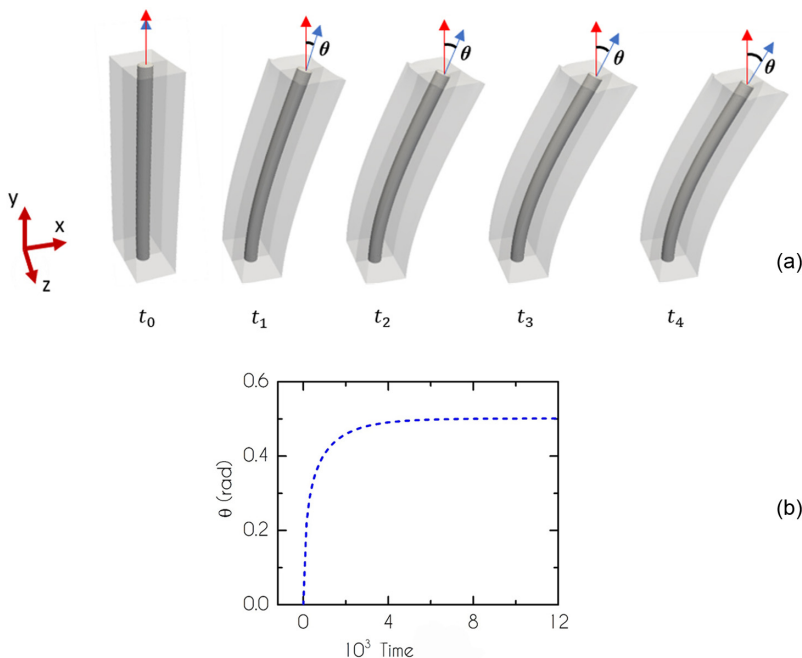


FIG. 5. (a) The transient response of EG fibers to a constant shear plasma flow at $t_0 = 0$, $t_1 = 1 \times 10^3$, $t_2 = 3 \times 10^3$, $t_3 = 6 \times 10^3$, $t_4 = 12 \times 10^3$. (b) Time evolution of the orientation angle of a fiber θ . All presented data were computed for $B_R = 0.33$, $H_K = 89$.

which for $B_R = 0.33$ and $H_K = 89$ is presented in Fig. 5(b). We notice the swift increase in θ from $\theta = 0$ at the very beginning of the simulation to $\theta = 0.502$ in steady state. The evolution of the angle is an exponential function of time. The cofactor of the dimensionless time is -261 , i.e., $\exp(-261t)$. Provided also the very small value of the characteristic time of the flow $O(5 \mu s)$, the relaxation time of the fiber motion is calculated to be of $O(19 \text{ ns})$. This means that the phenomenon is ultrafast and makes the accuracy of previous experimental studies questionable [38].

An advantage of the 3D configuration implemented herein is the direct calculation of the flow field in regions such as the interface between EG fibers and blood plasma, which are hardly accessible when utilizing other macroscopic approaches [13,31,39,40]. Indicatively, in Figs. 6(a) and 6(b), where we present the plasma streamlines past the glycocalyx fibers in top and side view, respectively, one can see that in the bulk of the EGL, plasma follows a path affected mainly by the spatial distribution of the fibers. At steady-state conditions, EG acts as an obstacle to the flow, allowing the plasma to traverse in the x -direction through the gap between adjacent fibers and leading to the development of notable gradients in the y - and z -directions, respectively. This hydrodynamic behavior is commonly encountered in flows past rigid cylinders or rigid objects in general. Moreover, due to the tilted cylindrical shape of the fibers, the flow field exhibits variations in each xz -plane in the y -direction. Over the fiber tips [Fig. 6(b)], which define the EGL-CFL interface, streamlines develop a periodic profile due to the low effect of inertia and the distribution of the deformed fibers. Also, we observe that plasma moves periodically from the CFL to the EGL and back. Studies of flowing liquids over slits and substrates [87] reveal similar hydrodynamic phenomena of fluid entrapment and periodic variations and demonstrate how periodic topography impacts the respective flow fields.

Our results regarding the plasma velocity magnitude are displayed in Figs. 6(c) and 6(d) for the characteristic planes at $y = 0.93A_R$ and $z = \sqrt{3}/B_R$, respectively. Inside the EGL, the plasma flows mainly in the x -direction and is intensified between the narrow spacing of the fibers, reaching up

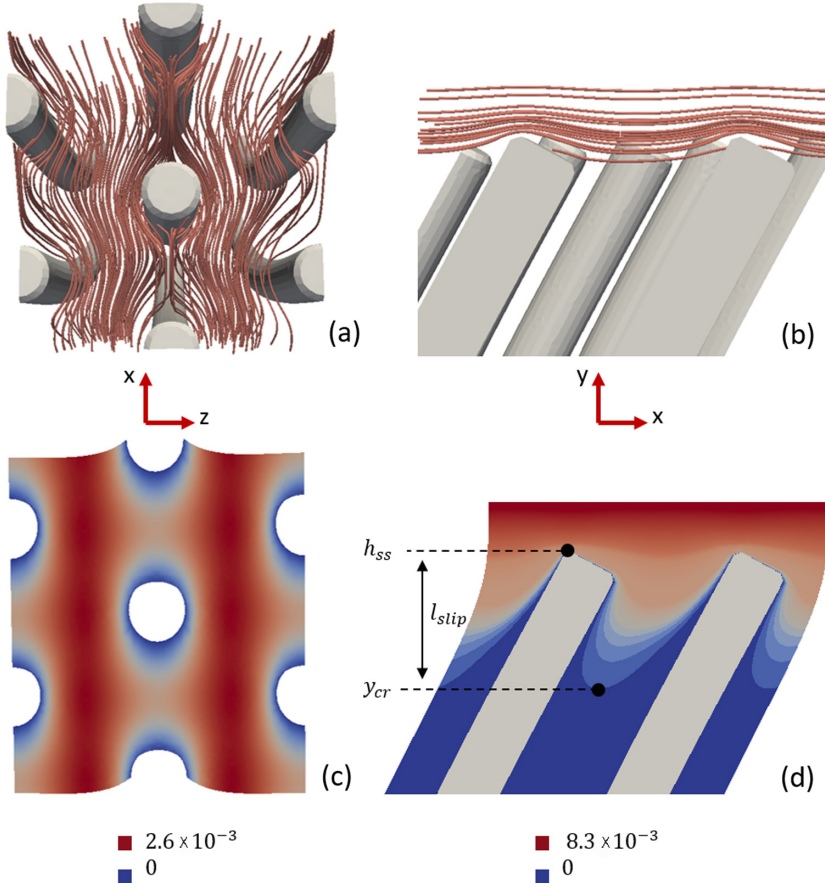


FIG. 6. (a) 3D top view of the plasma flow field in the EGL (looking from the top in the negative z -direction). (b) 3D side view of the plasma flow field over the EG fiber tips (looking from the right side in the negative z -direction). (c) Top view of the plasma velocity magnitude contours at $y = 0.93A_R$ (close to the fiber tips). (d) Side view of the plasma velocity magnitude contours at $z = \sqrt{3}/B_R$. The slip length l_{slip} is the vertical distance between the fiber tip and the point below where the plasma velocity is negligible. All presented data are at steady state for $B_R = 0.33$, $H_K = 89$.

to $u_{EGL}^{\max} = 2.6 \times 10^{-3}$. At the fluid-solid interface, the interaction of the two phases, subject to the no-slip/no-penetration restrictions, causes the plasma to have the same velocity as the fiber. Close to the fiber tips, one notices that the plasma velocity rapidly decreases as it enters the EGL, forming a distinct subdomain of EGL with a thickness in the y -direction known as *slip length* [88], in which the hydrodynamic phenomena are considered significant. By defining as y_{cr} the y -coordinate of the point at which the plasma velocity, u_{EGL} , starts becoming finite for the given discretization, e.g., $\frac{u_{EGL}}{u_{EGL}^{\max}} \geq \varepsilon = 10^{-2}$, we determine the dimensionless *slip length*, l_{slip} , as $l_{slip} = h_{ss} - y_{cr}$, where h_{ss} is the fiber height at steady state specifying also the EGL thickness in the y -direction [Fig. 6(d)]. The same feature has been studied by Hosoi [79] and is referred to as *penetration depth*. Based on her study, l_{slip} scales as $l_{slip} \sim \sqrt{\frac{\eta_{pm}K}{\eta_p R^2}}$ or $l_{slip} \sim \sqrt{k_{pm}}$, so it is reasonable to assume that l_{slip} can be approximated by

$$l_{slip} = C_1 \sqrt{k_{pm}} + C_2, \quad (26)$$

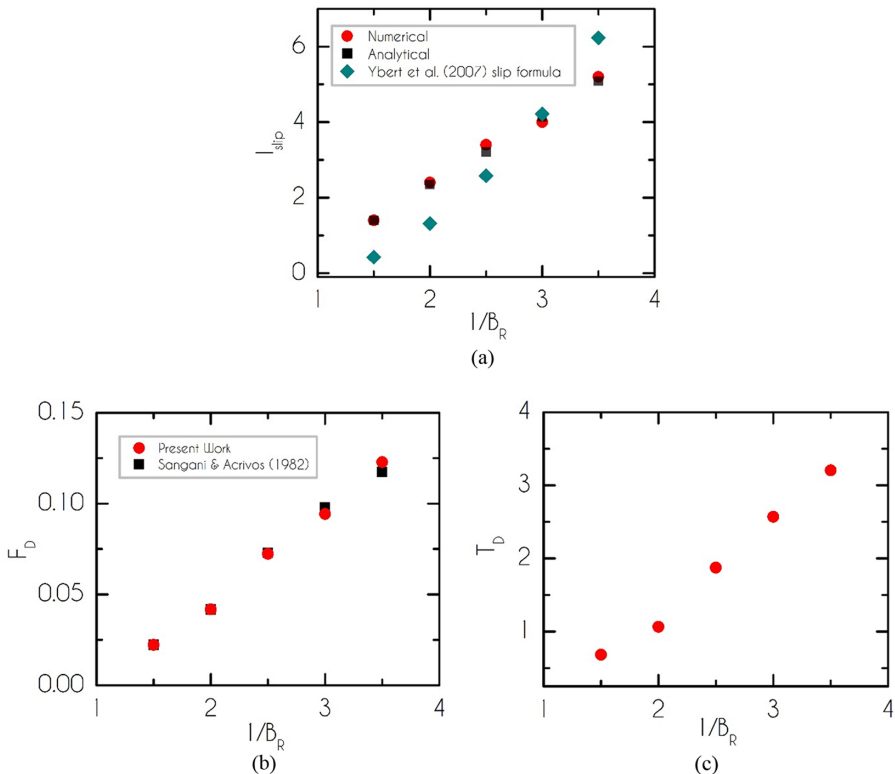


FIG. 7. (a) Slip length (l_{slip}), (b) drag (F_D), and (c) torque (T_D) at steady state for a range of B_R and $H_K = 89$. l_{slip} is compared to the one computed by Eq. (26). F_D is compared to the drag computed by the analytical expression of [26].

where C_1 , C_2 are constants to be evaluated. This is also proven in Appendix B. For different values of B_R , our numerical predictions for l_{slip} and k_{pm} suggest that Eq. (26) is satisfied for $C_1 = 3$ and $C_2 = 1$. In Fig. 7(a) we present our model predictions for l_{slip} at steady state for different values of B_R , and we compare them with those of Eq. (26) where k_{pm} is computed from Eq. (21) for the associated B_R values. For mildly deformable fibers, we confirm that l_{slip} scales linearly with the inverse of the blockage ratio $1/B_R$, for values up to 4. Consequently, under steady-state conditions, the drag force exhibits a similar linear dependence on $1/B_R$ [Fig. 7(b)], because only the flow within the slip layer exerts hydrodynamic forces on fibers. The same conclusion could be drawn if one examines Fig. 7(c), where the corresponding variation of torque (T_D) is shown.

The concept of the slip length has become the subject of systematic investigation due to its broad interest and its importance in micro- and nanofluid mechanics [89–91]. Herein we discuss if the $1/B_R$ dependence of l_{slip} ($= \hat{l}_{\text{slip}}/R_f$) is consistent with the findings of previous studies in different systems, which have major common features with our flow domain. According to Ybert *et al.* [91], at steady-state conditions, \hat{l}_{slip}/D varies linearly with $1/B_r$ in the limit of slow flow over a sparse bed of rigid circular posts under incomplete wetting conditions

$$\frac{\hat{l}_{\text{slip}}}{D} = \left(\frac{\hat{l}_{\text{slip}}}{R_f} \right) \left(\frac{R_f}{D} \right) = \frac{0.332}{\sqrt{\pi/4} B_r} - 0.421. \quad (27)$$

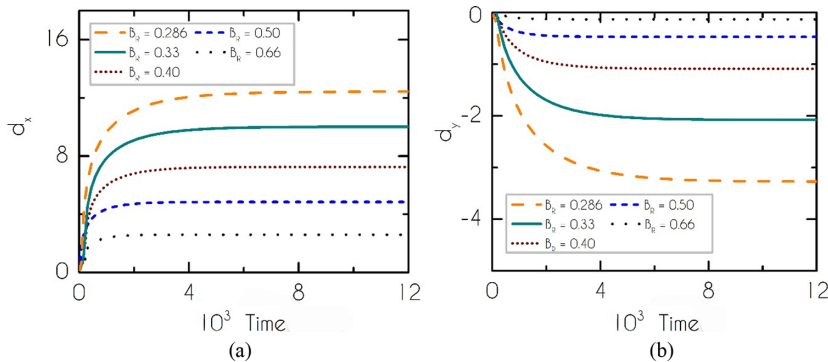


FIG. 8. The displacement components of the fiber tip (a) in the x -direction and (b) in the y -direction as functions of time for $B_R = 0.286, 0.33, 0.40, 0.50$, and 0.66 and $H_K = 89$.

If we rescale it by introducing the radius of the fiber, we get the following expression:

$$l_{\text{slip}} = \left(\frac{\hat{l}_{\text{slip}}}{R_f} \right) = \frac{0.664}{\sqrt{\frac{\pi}{4}} B_r^2} - \frac{0.842}{B_r}. \quad (28)$$

As we can also see in Fig. 7(a), the theory by Ybert *et al.* [91], and Davis and Lauga [89] can provide reasonable predictions for the variation of the dimensionless length scale for a wide range of the blockage ratio. However, there is an increasing deviation at the dense limit because of the $\frac{1}{B_r^2}$ term, which represents contributions from an inviscid substrate fluid (e.g., gas).

In order to quantify the EG response to the flow field, we measure the displacement of the fiber tip; the part of the fiber body, which is the most susceptible to deformations and whose location coincides with the dynamically changing EGL-CFL interface position. In Figs. 8(a) and 8(b), we present the evolution of the fiber-tip displacement components for different values of B_R . We notice that smaller values of the blockage ratio or larger gaps between the fibers are associated with a considerable increase in the displacement of the fiber tips since blood plasma has more space to flow freely, transferring larger amounts of momentum to the fibers.

Quite remarkable is the tracking of the EGL-CFL interface position and specifically the EGL compression resulting from the evaluation of the fiber tip displacement in the negative y -direction. This feature is extensively studied in [13,40] in simulations where the layer is crushed after the passage of red and white blood cells and left to recoil back to its steady state at simple shear flows. Even though their findings reveal the response of the layer to such intense hemodynamical conditions, the elasticity of the EG is several orders of magnitude larger than that suggested by later reports [63,77]. As a result, their models predict very small EGL compression caused exclusively by the shear plasma flow. On the contrary, our simulations for $B_R = 0.286$ demonstrate that the layer under shear flow is compacted more than 11% of its initial thickness in the y -direction.

The scaling of the components of the tip displacement vector under steady-state conditions is discussed extensively with the aid of the small deflection theory in Appendix B. There we show that d_x and d_y scale linearly and quadratically, respectively, with the inverse of the blockage ratio in the limit of sparse, porous media (see also Fig. 8). Another significant issue related to the deformation of the fibers is their structural stresses, which is discussed in Appendix C.

Figure 9 gives the space-averaged velocity \bar{U} of the mixed solid-fluid phase within the EGL as a function of time for different values of B_R . We observe that in short times, \bar{U} is substantially larger than in steady state. It is the motion of the fibers that due to their elasticity gets more restricted as time progresses and contributes to the decrease in \bar{U} . Particularly in steady state, the fibers are

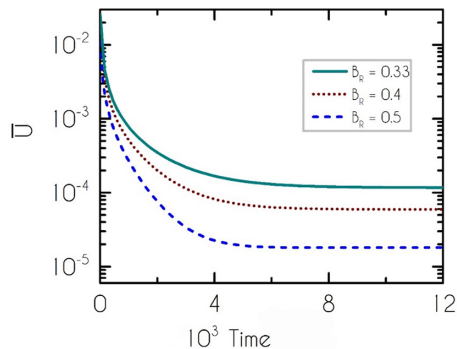


FIG. 9. Time evolution of the space-averaged velocity of the mixed solid-fluid phase within the EGL and for a step change in the shear-stress field and $B_R = 0.33, 0.4, 0.5$, and $H_K = 89$.

immobilized to their final deformed position maximizing their resistance to the flowing plasma. Moreover, our analysis suggests that a decreased B_R facilitates plasma traversal and favors the development of higher values of \bar{U} . Indicatively, for $B_R = 0.33$ and 0.5 , the values of \bar{U} differ by almost an order of magnitude. Plotting \bar{U} as a function of the blockage ratio at steady conditions, we observe that it scales quadratically with the inverse of the square of B_R . Thus, it is mainly affected by the compressive response of the glycocalyx layer, which is represented by the dependence of d_y on B_R .

In conclusion, this velocity field intensification with the reduction of the blockage ratio leads to the development of higher drag and torque produced by the flowing plasma on the EG (see also Fig. 7). Based on the analytical expression for the dimensionless drag proposed by Sangani and Acrivos [26] for the slow flow past a hexagonal periodic array of rigid cylinders, we compare our numerically computed drag F_D with their expression

$$F_D^* = \frac{4\pi}{\ln(c^{-0.5}) - 0.745 + c - \frac{c^2}{4}} h \bar{U}_p, \quad (29)$$

where c is the solid volume fraction and \bar{U}_p is the component of the calculated \bar{U} that refers only to the blood plasma phase and results from the numerical calculations. The corresponding data at steady state are presented in Fig. 7(b). The results of the numerical and analytical approaches are in very good agreement, revealing that the tilted cylindrical shape of the fibers is of little importance for the drag calculation. As we analytically show in Appendix B, the velocity component in the flow direction—which is the major factor to the magnitude of the drag force—decays exponentially within the glycocalyx. It takes nonzero values along the slip layer and scales inversely to the blockage ratio. Thus, the reduction of the height of the glycoproteins, which is accounted for in our simulations but was not taken into consideration in the derivation of Eq. (29) by Sangani and Acrivos [26], does not affect the slip length making the value of the drag-force at steady-state almost independent of the glycocalyx elasticity.

2. Effect of fiber elasticity

We proceed by varying H_K and maintaining the fibrous mesh size, and $B_R = 0.5$. In Figs. 10(a) and 10(b) we observe that d_x and d_y decrease hyperbolically with increasing H_K , which is also computed analytically in Appendix B. The absolute value of the curve slopes $|\frac{dd_x}{dH_K}|$ and $|\frac{dd_y}{dH_K}|$ increases at small values of H_K , suggesting that the EG elasticity alterations in this range strongly affect the fiber response to flow. For the extreme value of $H_K = 890$, the displacement of the fibers is negligible, leading to the conclusion that beyond that value of H_K , the elastic forces dominate over the viscous ones, making EGL stiff enough to be considered undeformable.

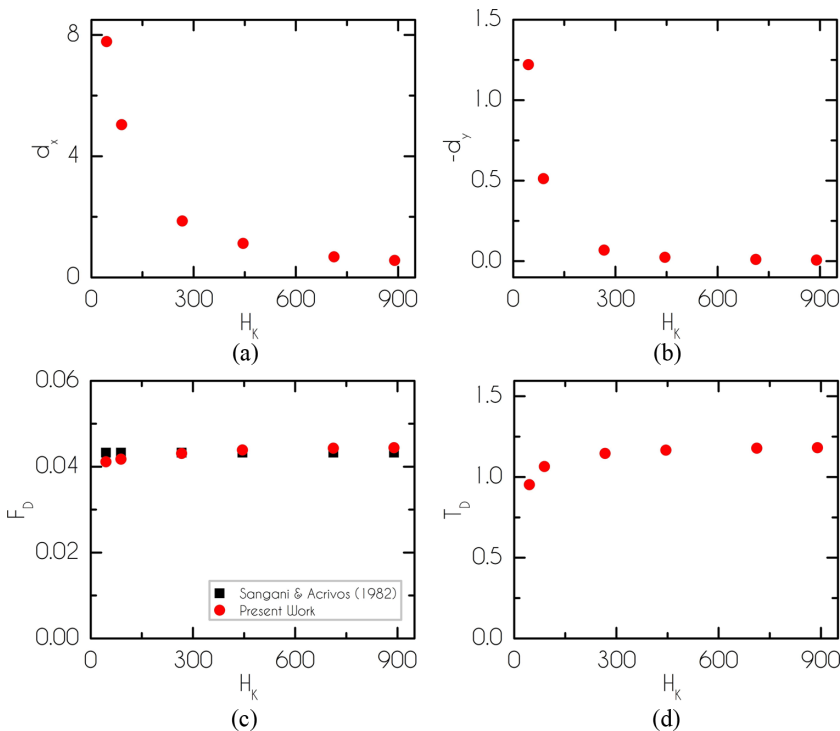


FIG. 10. (a), (b) Fiber-tip displacement components, (c) drag and (d) torque as functions of H_K at steady state for $B_R = 0.5$. Drag is compared to the one computed by the analytical expression of [26], which does not depend on H_K .

In Figs. 10(c) and 10(d), we summarize our results regarding F_D and T_D as well as the drag calculated from Eq. (29). Overall, we notice that F_D is consistent with the analytical expression in Ref. [26], taking values slightly higher than 0.04. Nevertheless, our findings indicate that the drag force is a slightly increasing function of H_K . This behavior is related to the deformed shape of the fibers, the upper free edge of which tends to align with the flow direction. This phenomenon is intensified as the viscous forces exceed the elastic ones, or else for decreasing H_K , causing the reduction of the surface area of the fibers opposing the flow and, consequently, the forces they are subjected to. With the reduction of the active surface area close to the fiber tips, the hydrodynamic load distribution on more easily tilted cylindrical bodies is concentrated around a point much lower (in the y -direction) than the corresponding point load of more stiff ones. For this reason, the reduction rate of the torque with decreasing H_K is larger compared to that of the drag.

3. Apparent permeability

The EGL dimensionless effective permeability of the glycocalyx as a function of time is presented in Figs. 11(a) and 11(b) for different B_R and H_K , respectively. At steady state the flexibility of EG does not seem to affect significantly the EGL apparent permeability k_{pm} . In particular, the parametric studies regarding H_K and B_R suggest that at steady state, k_{pm} has approximately the same value with rigid fibers ($H_K \rightarrow \infty$). Plotting k_{pm} versus B_R , we conclude that the former is inversely proportional to the square of the latter. This is another indication of the impact of the vertical bending motion of the glycoproteins in the average quantities of the fibrous layer.

Nonetheless, at the beginning of our simulations, we observe that k_{pm} is two to three orders of magnitude higher than at steady state because then the fibers are free to move, and the plasma

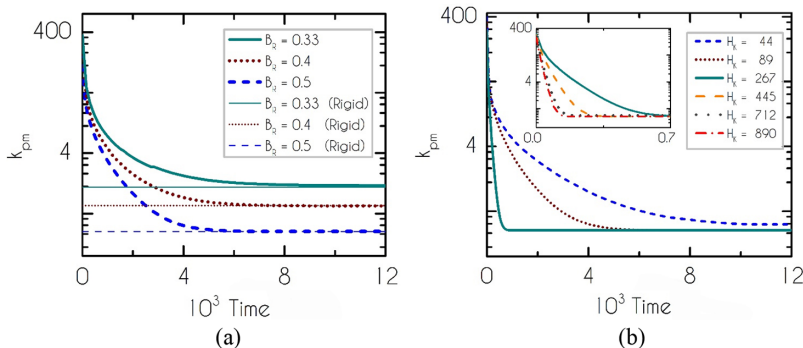


FIG. 11. The EGL transient apparent permeability as a function of time for (a) $B_R = 0.33, 0.4, 0.5$ and $H_K = 89$, and (b) $B_R = 0.5$ and $H_K = 44\text{--}890$ for start-up shear.

traversal is favored. Considering that the duration of the fiber motion increases as H_K decreases, we observe that the slope of k_{pm} decreases as well. Consequently, we conclude that when the flexible fibers can move and deform, the ability of the EGL to allow fluid transition intensifies and that this ability is increased as the viscous effects overwhelm the elastic ones, or else, as H_K decreases.

B. Pulsating shear

1. Local dynamics and effect of blockage ratio

The second part of our analysis involves the oscillatory shear flow, which simulates the pulsatile blood flow in large and small vessels, but it also represents the oscillatory rheometric protocol ([81,84]). Typical waveforms of the blood flowrate found in the literature [92–94] suggest that vessel-core velocity oscillates between zero and a finite value A_m within a period T^* . Approximating this waveform by a sinusoidal function of time (t^*) of the form $A_m \sin^2(\frac{\pi t^*}{T^*})$, we assume that the transient velocity on the CFL-core interface is expressed as $V'_{\text{CFL}} = V_{\text{CFL}} \sin^2(\pi t^*) [\frac{mm}{s}]$, where $T^* = 1$ s (this corresponds to the typical human pulse of 60 bpm) and we set $u_p^{\text{top}} = \frac{V'_{\text{CFL}}}{V_{\text{CFL}}}$. Now, the imposed dimensionless velocity on the top boundary oscillates from zero to unity within a period $T = \frac{V_{\text{CFL}}}{R_f}(T^*)$ and the plasma-glycocalyx system is monitored for three periods, neglecting any phase difference between the vessel-core velocity and u_p^{top} , due to blood thixotropic phenomena [95–98]. The parametrization of the waveform represents the hemodynamics encountered in a small vessel of a healthy human individual in a physiological state, where their heart beats with a 60 bpm pulse.

The fiber response to the plasma flow is presented in Fig. 12(a) (see also the Supplemental Material, movie 2 [86]). It should be mentioned that the initial transient effects are not shown, but we focus our discussion on the periodic state. Glycocalyx fluctuates periodically between its initial undeformed state and a position of maximum deflection in the flow direction, while the same frequency and phase describe its motion as u_p^{top} . Besides the different evolution over time, the fiber configurations resemble those predicted for steady shear, which are also characterized by bending with notable fiber orientation changes. The impact of oscillatory plasma flow on the EG's orientation is displayed in Fig. 12(b) for the same $B_R = 0.33$ and $H_K = 89$. We notice a sinusoidal temporal evolution in θ from $\theta = 0$ when $u_p^{\text{top}} = 0$ to $\theta = 0.52 \cong \pi/6$ when $u_p^{\text{top}} = 1$.

The simulations under oscillatory flow conditions reveal some very interesting features that make it significantly different from unidirectional flows (e.g., start-up shear). One of them is related to the time evolution of space-averaged quantities (e.g., velocities) in the EGL. In Fig. 13(a) we present the time evolution of the space-averaged velocity of the fibers (\bar{U}_f), the plasma (\bar{U}_p), and the fiber-plasma combined (\bar{U}) in the control volume of EGL with $B_R = 0.33$ and $H_K = 89$. Four

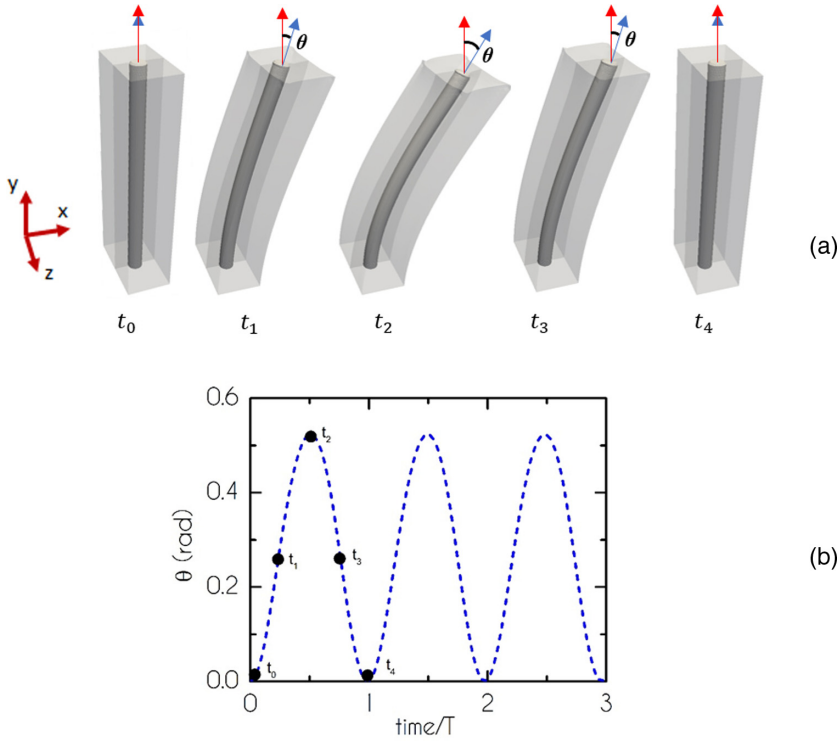


FIG. 12. (a) The transient response of a single fiber to pulsatile plasma flow in a period, T , for $B_R = 0.33$ and $H_K = 89$ at $t_0 = 0$, $t_1 = 0.25T$, $t_2 = 0.5T$, $t_3 = 0.75T$, $t_4 = T$. (b) The evolution of the orientation angle θ in time in three periods.

distinct time segments characterize the fiber motion through a period. From $t = 0$ to $t = 0.22T$, \bar{U}_f increases monotonically from $\bar{U}_f = 0$ reaching its maximum $\bar{U}_f = 1.02$. In this timespan, the hydrodynamic forces dominate over the fiber's elastic ones causing an acceleration until $t = 0.22T$, when equilibrium is established. Next, even though the main bloodstream continues to accelerate, the accumulated stress inside the fibers generates an opposite force that overwhelms the hydrodynamic one leading to fiber deceleration. The EG velocity decreases to zero at $t = 0.5T$, which is the time when the main bloodstream velocity is maximized, and the fibers acquire their fully deformed shape. The fibers accelerate in the opposite direction to the main bloodstream until the appearance of a second stationary point at $t = 0.77T$. Up to this instant, most of the stresses stored in the elastic fibers have been released through the recoil to their initial position, and the hydrodynamic load begins to dominate once again. After $t = 0.77T$, the EG gradually returns to its undeformed state with a descending negative velocity, and the whole cycle starts over at $t = T$.

Regarding the plasma velocity dynamics, at the beginning of the cycle, \bar{U}_p increases due to the flow of the main bloodstream [Fig. 13(a)]. However, the fiber elasticity opposes viscous stresses and \bar{U}_p reaches its peak of 1.9 around $t = 0.36T$, much earlier than the maximization of the imposed velocity. From this point on, \bar{U}_p descends passing through zero at $t = 0.68T$ where the effect of the two forces on the flowing plasma balance each other. In the time window $t \in (0.68T, T)$, the plasma inside the EGL is swept away by the recoiling fibers in the opposite direction to the main bloodstream.

Provided that the plasma occupies most of the space inside the EGL, \bar{U} as a function of time is only slightly different from \bar{U}_p . Nonetheless, the influence of the fibers is perceived through the development of a backflow caused by their recoil, even though far from the EGL, blood flows solely

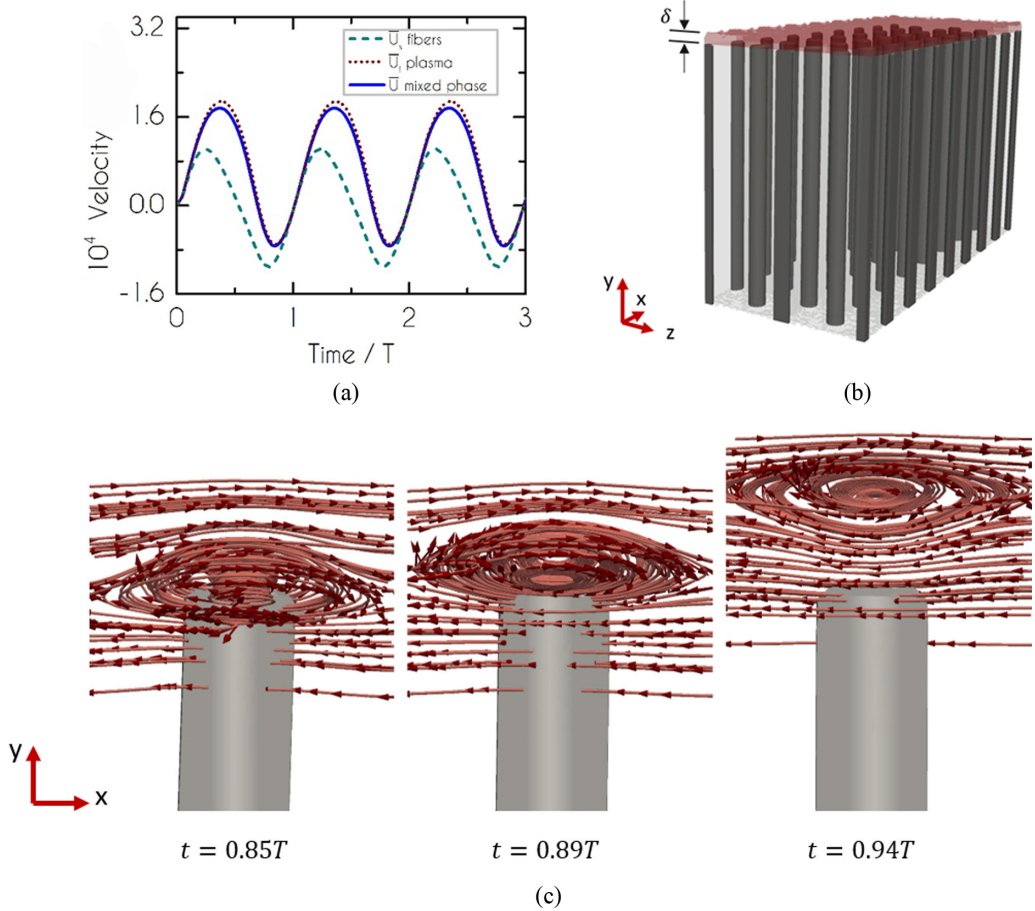


FIG. 13. (a) Time evolution of the space-averaged velocity of the fibers, the plasma, and the fiber-plasma pair combined inside the EGL under oscillatory blood flow at 60 bpm. (b) An illustration of the backflow region, which extends over the fiber tips and inside the CFL with a thickness $\delta(t)$. At $t = 0.94nT$ the thickness of the backflow region inside CFL takes its max value, $\delta(t = 0.94nT) = 1.35R$. (c) The time evolution of the plasma recirculation. The center of the vortex is located on the border between the backflow generated by the fiber and the main plasma region and keeps moving forward and above the fiber tip. All presented data were computed for $B_R = 0.33$ and $H_K = 89$.

in the positive direction. This is another notable feature of the oscillatory flow. There are times within a period that the phenomenon of the reversed plasma flow extends from the interior of the EGL to a small region of the CFL, the so-called *backflow region* [Fig. 13(b)]. When the reversed flow appears inside the CFL for the first time, the backflow region is confined just on top of each fiber. In contrast, when it is maximized, it also occupies a space of finite thickness in the y -direction, δ , and extending in x - and z -directions throughout the domain. Specifically, the corresponding region appears at $t = 0.85nT$, where $n = 1, 2, \dots$, [Fig. 13(c), left], which is maximized just before the end of each period at $t = 0.94nT$ [Fig. 14(c), right] with $\delta = 1.35R_f$, and then vanishes at $t = nT$. Between the backflow region and the region of the main plasma flow, the plasma is locally recirculating. The center of each recirculation is located on the border of the respective areas and above each fiber tip, where the effect of the fiber recoil is enhanced. The lifespan of the vortices coincides with that of the reversed flow inside the CFL.

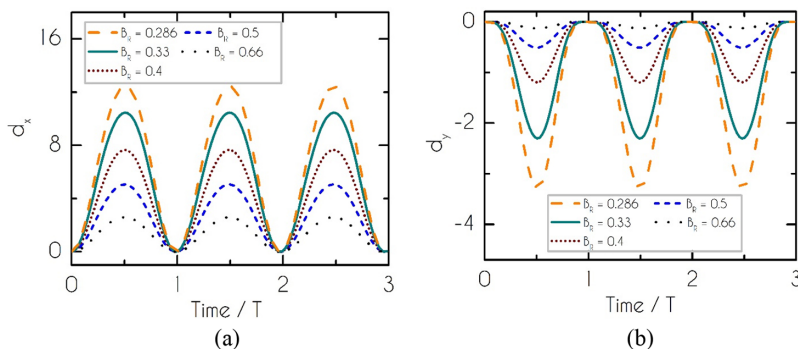


FIG. 14. The dimensionless fiber-tip displacement, x -component (a) and y -component (b) as functions of time for $B_R = 0.286, 0.33, 0.4, 0.5$ and 0.66 , and $H_K = 89$.

The displacement of the fibers measured at their free edges demonstrate a symmetric evolution over time with the same frequency and phase as V_{CFL} . Figure 14 gives the corresponding displacement components as functions of time for a glycocalyx matrix of various B_R and $H_K = 89$. We observe that any decrease in B_R increases the fiber-tip displacement in both directions. In particular, when the central bloodstream velocity is maximized, d_x and d_y reach up to 2.6, 5.0, 7.7, 10.5, and 12.4, and $-0.13, -0.5, -1.2, -2.3,$ and -3.3 for $B_R = 0.286, 0.33, 0.4, 0.5,$ and 0.66 , respectively. Considering that negative vertical fiber-tip displacement indicates EGL compaction, our results reveal that the layer is compressed by the oscillatory shear plasma flow up to $0.11A_R$, or else, 11% of its original y -directional thickness for $B_R = 0.286$.

A display of the combined fluid-solid phase \bar{U} as a function of time for different blockage ratio is given in Fig. 15. The simulations show that \bar{U} evolves sinusoidally and symmetrically in time with the same frequency as u_p^{top} and a shifted phase and amplifies with decreasing B_R . Provided that smaller blockage ratios (B_R) result in larger EG deformations (Fig. 14) due to stronger hydrodynamic load, the fiber displacement in the direction of the flow is enhanced. Hence, more deflected fibers require larger amounts of fluid momentum hence higher velocity in the negative x -direction to return to their initial position at the end of each cycle. In spacious EGL matrices, these mechanisms are responsible for the development of smaller minimum values of negative \bar{U} and the reduction of the duration $\Delta t_{\text{backflow}}$, in which \bar{U} is reversed. Furthermore, the effect of fiber elasticity on the hydrodynamics of the EGL is minimized when the latter becomes more dilute (lower values of B_R), resulting in a reduction in the phase discrepancy between the transient profile of \bar{U} and u_p^{top} . Specifically, decreasing B_R causes \bar{U} to reach its extreme values at instants t_{max} and

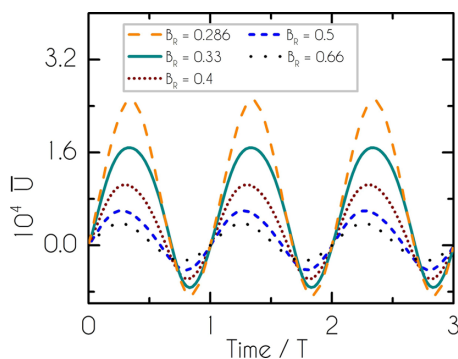


FIG. 15. EGL mixed-phase velocity \bar{U} as a function of time for different B_R , and $H_K = 89$.

TABLE III. Maximum, \bar{U}_{\max} , and minimum, \bar{U}_{\min} , values of the velocity of the plasma-fibers system combined and the corresponding time instants, t_{\max} and t_{\min} , for different B_R . $\Delta t_{\text{backflow}}$ is the lifespan of the backflow. t_{\max}^{top} and t_{\min}^{top} refer to the instants where the imposed u_p^{top} acquires its extreme values.

B_R	$\bar{U}_{\max} \times 10^4$	t_{\max}	t_{\max}^{top}	$\bar{U}_{\min} \times 10^4$	t_{\min}	t_{\min}^{top}	$\Delta t_{\text{backflow}}$
0.286	2.5	$0.35T$	$0.5T$	-0.84	$0.85T$	$1.0T$	$0.30T$
0.33	1.7	$0.33T$	$0.5T$	-0.73	$0.82T$	$1.0T$	$0.32T$
0.4	1.0	$0.29T$	$0.5T$	-0.60	$0.79T$	$1.0T$	$0.35T$
0.5	0.6	$0.26T$	$0.5T$	-0.40	$0.77T$	$1.0T$	$0.40T$
0.66	0.4	$0.25T$	$0.5T$	-0.27	$0.75T$	$1.0T$	$0.46T$

t_{\min} , which deviate less from those corresponding to u_p^{top} . The corresponding data are summarized in Table III.

Figure 16 depicts drag and torque on a fiber as a function of time for the corresponding B_R values. Similar to the behavior of the velocity averages, both measures demonstrate a periodic and symmetric evolution in time, which is in phase with u_p^{top} . Consistently with the findings of the start-up shear analysis, it is indicated that drag and torque are magnified due to the intensification of the flow field (Fig. 15). An overview of the measured data is presented in Table IV. We observe a reduction in the exerted maximum drag and a smaller reduction in the maximum torque. This can be attributed to the displacement of the fiber in the negative y -direction, which causes drag to concentrate around a point closer to the EG base. If y_{point} is the y -coordinate of the point load on the fiber's body, then in the case of elastic fibers, the torque is not linearly dependent on drag, because in the relation $T_D = F_D \times y_{\text{point}}$ the length y_{point} is not constant under varying B_R .

The variation of l_{slip} in time is displayed in Fig. 17. At the beginning and the end of each cycle, l_{slip} takes values that are about one order of magnitude higher than the corresponding values at the middle of the period when the fiber deflection is maximized. In terms of analytical expressions, l_{slip} is proportional to the instantaneous aspect ratio $A_R(t)$ of the fiber, which is in proportion to the vertical displacement [Fig. 14(b)]. Thus, at the time of maximum deflection, the fibers are immobile, and the penetration of blood plasma is limited. However, to provide the total impact of the fiber movement under these flow conditions on l_{slip} , we calculate the time-averaged slip length, $\langle l_{\text{slip}} \rangle = \int_0^{3T} l_{\text{slip}}(t) dt / 3T$, which is presented in Fig. 17(b) for different values of B_R . In pulsatile flow and when the fibers motion is accounted for, our results indicate that $\langle l_{\text{slip}} \rangle$ can be one order of magnitude greater. In that case, $\langle l_{\text{slip}} \rangle$ is a linear function of the inverse of the blockage ratio that is given by

$$\langle l_{\text{slip}} \rangle (B_R) = 1.21/B_R + 9.73. \quad (30)$$

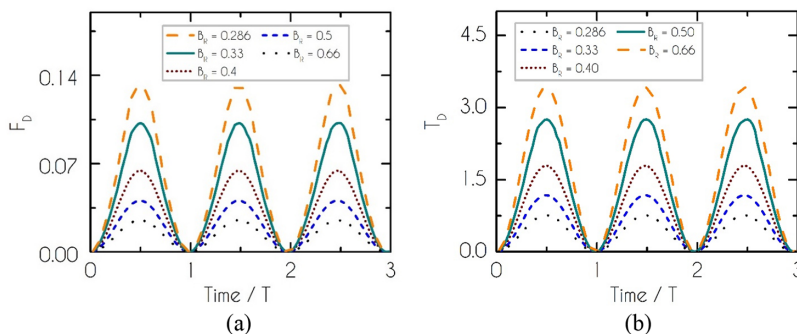


FIG. 16. (a) Drag and (b) torque on a fiber as a function of time for $B_R = 0.286, 0.33, 0.4, 0.5,$ and 0.66 and $H_K = 89$.

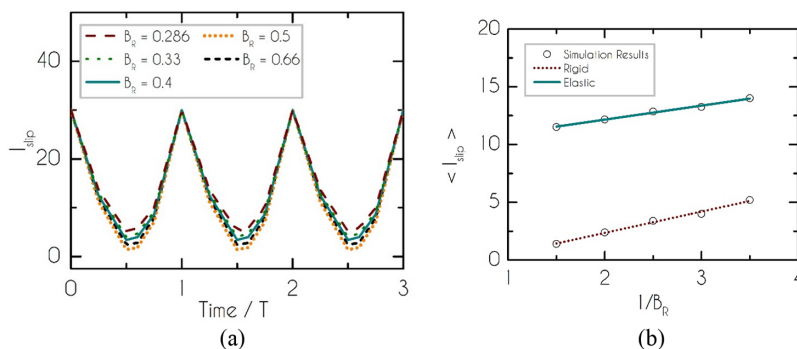
TABLE IV. Maximum drag, $F_{D,\max}$, and torque, $T_{D,\max}$, for different B_R , and $H_K = 89$. y_{point} refers to the y -coordinate of the equivalent point load of $F_{D,\max}$.

B_R	$F_{D,\max}$	$T_{D,\max}$	y_{point}
0.286	0.131	3.44	$0.87A_R$
0.33	0.103	2.73	$0.90A_R$
0.4	0.065	1.78	$0.92A_R$
0.5	0.041	1.17	$0.96A_R$
0.66	0.025	0.74	$0.99A_R$

2. Effect of fiber elasticity

Here we study of the role of H_K on the dynamics of the system under pulsatile flow conditions. Specifically, in Figs. 18(a) and 18(b), we present the measured fiber-tip displacement components over the course of three cycles for EG fibers for $B_R = 0.50$, and $H_K = 8.9$ – 890 . We observe that irrespective of H_K , both d_x and d_y follow the pattern in startup shear flow, but here evolving periodically and symmetrically in time with the same frequency and phase as u_p^{top} . However, deviation from the sinusoidal evolution appears at low values of H_K . For smaller H_K , where the viscous effects of the flowing plasma overwhelm the elasticity of the fibrous array, the flexible cylinders demonstrate large displacements in both directions. Additionally, a decrease in H_K is related to a faster response of the fibers to the oscillatory plasma flow denoted by a monotonous increase in the slope of d_x and d_y as functions of time as visualized in the vicinity of the beginning of each period. Regarding the EGL compression, our simulations predict that the layer is compacted up to $0.08A_R$, or 8% of its initial thickness for $H_K = 8.9$.

The temporal variation of the mixed-phase velocity \bar{U} inside the EGL is presented in Fig. 19 for different values of EG elasticity. A reduction in E_f causes the increase of the mixed-phase velocity \bar{U} , agreeing with the pattern found with the start-up protocol in Fig. 11. However, for high enough values of the ratio H_K , we observe that \bar{U} evolves symmetrically in time, whereas for $H_K \leq 89$ asymmetry arises. Particularly in the cases where H_K is smaller, maximum and minimum values of \bar{U} appear near the start and the end of each period, respectively, and the temporal gap that separates the corresponding instants is increased. The lifespan of the backflow, $\Delta t_{\text{backflow}}$, does not depend monotonically on H_K being truncated both for high and small H_K values (Table V). The phenomenon of reversed flow inside the EGL (and occasionally in the bottom part of the CFL) due to the fibers' recoil results from their elasticity. Consequently, for the asymptotic cases of (a) totally


 FIG. 17. Evolution of the slip length l_{slip} for different B_R and $H_K = 89$.

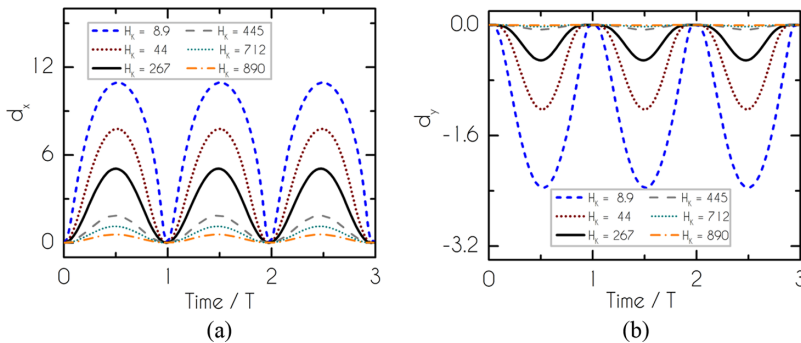


FIG. 18. (a) Fiber-tip x - and (b) y - displacement components as functions of time for $B_R = 0.50$, $H_K = 8.9$ – 890 .

rigid EG fibers ($H_K \rightarrow \infty$) and (b) fibers that are unable to maintain their structural integrity under shear flow ($H_K \rightarrow 0$), it is expected that no negative \bar{U} would develop and $\Delta t_{\text{backflow}} \rightarrow 0$.

For very small H_K ratios and during the reversed motion of fibers, large deformations induce the emergence of intense negative \bar{U} whose magnitude occasionally surpasses the corresponding maximum positive value. In particular, for $H_K = 8.9$, the absolute value of \bar{U}_{min} is over 152% larger than \bar{U}_{max} (Table V). For the cases that \bar{U}_{min} surpasses \bar{U}_{max} , the highly deflected EG (small H_K) develops amplified velocity to recoil back to its initial position shortly thereafter. However, this phenomenon should not be misinterpreted as a negative \bar{U} over a period. To support this statement and avoid any misconception, we present the time-averaged $\bar{U}(t)$ as $\langle \bar{U} \rangle = \int_0^{3T} \bar{U}(t) dt / 3T$ in Table V, which is evidently positive in all cases.

The transient evolution of drag and torque on a fiber for different values of H_K is presented in Fig. 20. Both are in phase with u_p^{op} . The effect of variations in H_K on the drag is negligible in the range $H_K \in [8.9, 890]$. However, because of the vertical displacement of the fibers, we notice that around $t = T/2$, the torque is negatively affected when the fibers become more flexible. As previously discussed, the drag on highly bent fibers is accumulated closer to their base and results in reduced torque. Information about the computed data is outlined in Table VI. We observe a remarkable deviation over 13.5% to the maximum torque between the extreme cases of $H_K = 8.9$ and $H_K = 890$, even though the drag remains constant.

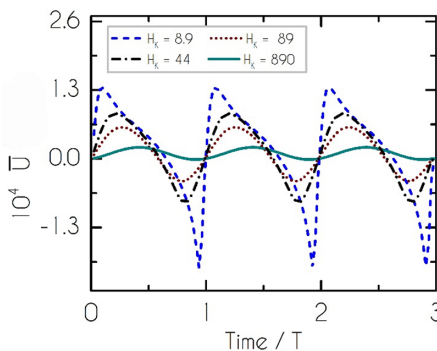


FIG. 19. EGL mixed-phase velocity \bar{U} as a function of time for $B_R = 0.50$, $H_K = 8.9$ – 890 .

TABLE V. Maximum, \bar{U}_{\max} , and minimum, \bar{U}_{\min} , values of the velocity of the plasma-fibers pair combined and the corresponding time instants, t_{\max} and t_{\min} , for $B_R = 0.50$, and $H_K = 8.9$ –890. $\Delta t_{\text{backflow}}$ is the duration of the backflow. t_{\max}^{top} and t_{\min}^{top} refer to the instants where the imposed u_p^{top} acquires its extreme values.

H_K	$10^4 \times \bar{U}_{\max}$	t_{\max}	$t_{\max}^{\text{Vcfl}} [\text{s}]$	$10^4 \times \bar{U}_{\min}$	$t_{\min} [\text{s}]$	$t_{\min}^{\text{Vcfl}} [\text{s}]$	$\Delta t_{\text{backflow}} [\text{s}]$	$10^4 \times \langle \bar{U} \rangle$
8.9	1.34	$0.096T$	$0.5T$	-2.05	$0.938T$	T	$0.33T$	0.19
44	0.86	$0.216T$	$0.5T$	-0.83	$0.818T$	T	$0.39T$	0.02
89	0.60	$0.265T$	$0.5T$	-0.42	$0.770T$	T	$0.40T$	0.01
890	0.22	$0.409T$	$0.5T$	-0.13	$0.914T$	T	$0.16T$	0.01

3. Apparent permeability

Consistently with the EGL mixed-phase velocity, the transient apparent permeability demonstrates asymmetric oscillations (Fig. 21). Specifically, the minimum values of k_{pm} appear when the EG fibers are close to their most deformed state, and their resistance to the flow is maximized. On the contrary, the maximum k_{pm} occurs when they are almost undeformed and flexible to move in the direction of the plasma flow, underlining that the EG flexibility favors the EGL apparent permeability. In terms of the model parameters, k_{pm} monotonically increases with increasing B_R and decreasing H_K . To quantify this behavior, we introduce the time-averaged apparent permeability $\langle k_{pm} \rangle = \int_0^{3T} k_{pm}(t) dt / 3T$. In Fig. 22(a) the dependence of $\langle k_{pm} \rangle$ on B_R is compared to the case of totally rigid fibers. For moderate or high values of the fiber elasticity, the time-averaged $\langle k_{pm} \rangle$ exhibits a monotonic dependence on B_R , but with significantly different rates of growth. More importantly, our results suggest that when the fiber flexibility is accounted for, $\langle k_{pm} \rangle$ can be more than one order of magnitude higher than that for undeformed fibers. Also, we notice that the growth rate of $\langle k_{pm} \rangle$ as a function of $1/B_R$ is increased for the case of elastic fibers. This observation can be justified considering that a broadening of the gap between adjacent fibers intensifies their resulting displacement in time (Fig. 14) or equivalently their velocity. The fiber velocity favors the mixed fiber-plasma velocity inside the EGL and consequently increases $\langle k_{pm} \rangle$ [Eqs. (17)–(20)]. This phenomenon is absent in the case of rigid bodies, and the only mechanism that affects $\langle k_{pm} \rangle$, when B_R varies, is purely geometrical. The least-square fitting of $\langle k_{pm} \rangle$ as a function of B_R is given by

$$\langle k_{pm} \rangle (B_R) = 0.89 / B_R^2 - 1.07 / B_R + 1.18, \quad (31)$$

where $B_R \in [0.286, 0.66]$ and $H_K = 89$.

The impact of the fiber elasticity on the permeability of the EGL is presented in Fig. 22(b). We notice that in the limit of $H_K \rightarrow 0$, $\langle k_{pm} \rangle$ tends to become asymptotically large, corresponding to a nonporous medium, where resisting forces due to solid obstacles are absent. For large values of

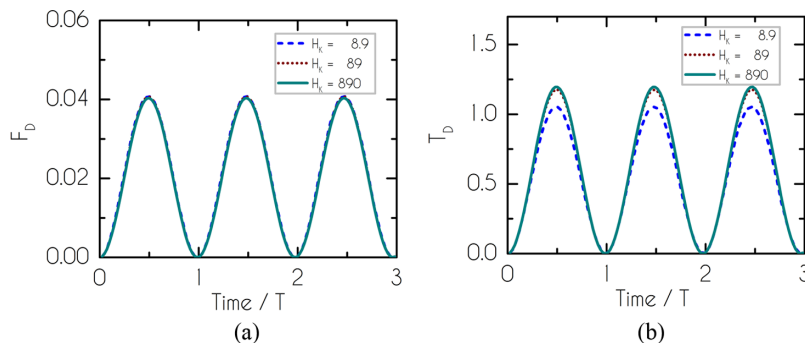


FIG. 20. (a) Drag and (b) torque on a fiber as functions of time for $B_R = 0.50$, $H_K = 8.9$ –890.

TABLE VI. Maximum drag, $F_{D,\max}$, and torque, $T_{D,\max}$, for $B_R = 0.50$, $H_K = 8.9\text{--}890$. y_{point} refers to the y -coordinate of the equivalent point load of $F_{D,\max}$.

H_K	8.9	44	267	445	712	890
$F_{D,\max}$	0.04	0.04	0.04	0.04	0.04	0.04
$T_{D,\max}$	1.04	1.11	1.16	1.18	1.19	1.19
y_{point}	$0.87A_R$	$0.93A_R$	$0.96A_R$	$0.98A_R$	$0.99A_R$	$0.99A_R$

H_K , the permeability $\langle k_{pm} \rangle$ asymptotically reaches the value related to a layer consisting entirely of rigid cylindrical fibers, which are spatially distributed in a hexagonal pattern. As our findings reveal, $\langle k_{pm} \rangle$ is a rational function of H_K of the form

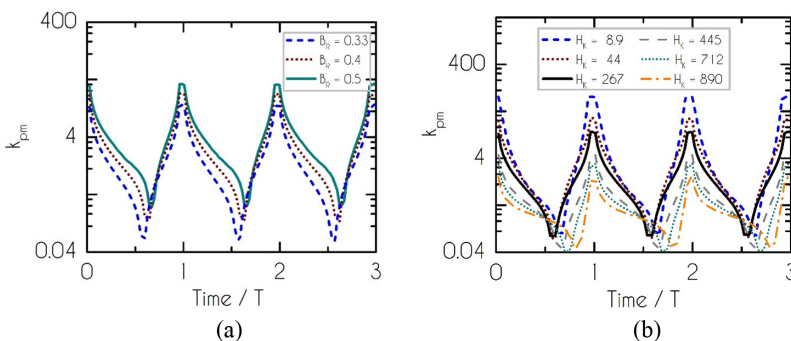
$$\langle k_{pm} \rangle(H_K) = (6.8 \times 10^{-7} H_K^2 + 3.7 \times 10^{-3} H_K + 4.5 \times 10^{-2})^{-1}, \quad (32)$$

where $H_K \in [8.9, 890]$ and $B_R = 0.5$. Expressions like Eq. (31) and (32) are very useful for conducting continuous multilayer modeling and simulation in networks of microvessels, where the role of EGL is critical since it controls the hemodynamics [98] (e.g., apparent viscosity of blood) and the homeostasis of the tissue.

V. CONCLUSIONS

A 3D model has been developed for studying the fluid dynamics of a Newtonian fluid through an array of flexible hyperelastic fibers in a periodic hexagonal arrangement. Specifically, the analysis is focused on the dynamics of the EGL and the kinematics of the surrounding blood plasma under start-up and oscillatory flow conditions featuring a fluid-structure interaction (FSI) algorithm. Our model incorporates the material properties of the corresponding phases and an elementary geometrical configuration that builds the EGL physical domain through the concepts of symmetry and periodicity. Under more typical physiological conditions (pulsatile flow), our findings reveal that the motion of the elastic fibers heavily affects the hydrodynamics of the circulating blood plasma, the respective layer's instantaneous thickness, and its ability to allow fluid permeation. In contrast to previous theoretical works [13,85,99], they also reveal that the two-way coupling of the solid and fluid balances is necessary for reproducing all relevant phenomena accurately.

The model allows us to draw conclusions about the dynamics of individual fibers and the whole system. Under constant shear blood flow, the total hydrodynamic drag exerted on a fiber is relatively unaffected by the variations of the shear modulus, but it is augmented when the fiber matrix becomes denser. At long times, when steady state conditions have been established, we found that the


 FIG. 21. The dimensionless apparent permeability of the EGL as a function of time (a) for $B_R = 0.33, 0.4, 0.5$ and $H_K = 89$, and (b) for $B_R = 0.5$, and $H_K = 8.9\text{--}890$.

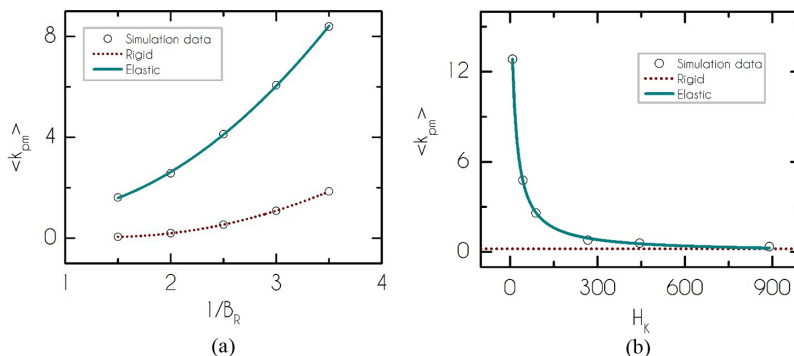


FIG. 22. Time-averaged apparent permeability of the EGL as a function of (a) $1/B_R$ and (b) H_K and comparison with the corresponding permeability of totally rigid fibers.

drag force can be approximated by the analytical expression of Sangani and Acrivos [26] for the case of hexagonal periodic arrays of cylinders, but this expression fails to represent the transient phase accurately. On the other hand, the total hydrodynamic torque on a fiber is an increasing function of both elasticity (H_K) and blockage (B_R) ratio. For the examined range of flow and structural parameters, the elevated values of hydrodynamic forces applied on the EGL fibers move them in the flow direction and bend them vertically downwards at 11% from their initial height. Also, the vertical squeeze of the fibers temporarily increases under oscillatory flow conditions and has multiple implications in the macroscopic response of the EGL (e.g., apparent permeability). Regarding the periodic regime, the total hydrodynamic drag and torque on a fiber exhibit a periodic temporal evolution in phase with the imposed plasma flow. Both flow measures, as functions of B_R and H_K , present the same behavior detected in the analysis under constant shear flow.

In general, the two flow protocols exhibit similarities but also significant distinctions in the evolution of the flow features. In both cases, the development of a slip layer within the upper part of EGL guarantees that the membrane of endothelial cells is slightly sheared by the plasma, while fibers are essential elements for transmitting the mechanical signal to the cytoskeleton of the endothelial cells [100]. It should be mentioned that at a steady state, the thickness of the slip layer (or the slip length) inside the EGL scales with the square root of the dimensionless apparent permeability or the inverse of the blockage ratio B_R . These findings are consistent with the predictions of our analytical model based on the linear beam deflection theory presented in Appendix B as well as with the boundary layer approximation proposed by Hosoi [79]. Regarding the permanent reduction of the EGL height, $-d_y$, it scales as B_R^{-2} , while the permanent horizontal extension d_x , it scales as of B_R^{-1} for a fixed value of the elasticity number. The space-averaged velocity \bar{U} in the EGL and the dimensionless apparent permeability follow the same scaling law as d_y , implying that its compressive response controls the flow dynamics in the layer. For fixed spacing of the glycoproteic fibers, both components of the tip displacement vector vary as H_K^{-1} .

Above the EGL, the local flow field can be strongly affected by the imposed flow and the mechanical characteristics of the fibers. In the start-up shear field, the velocity field varies almost linearly along with the CFL, but in the proximity of the CFL-EGL interface denoted by the fiber tips, the plasma alternately transitions from CFL to EGL, enhancing the mixing of the contained proteins. When a pulsating flow is imposed, a thin backflow layer is developed above the fiber tips, its area varies within a cycle, and its thickness is of the order of the fiber radius. The layer is formed because of the hydrodynamic interaction of the plasma inside and on top of the EGL, which evolves periodically in time with different phases from the imposed oscillatory plasma flow, with the recoiling fibers, which results in a backflow.

Compared to the case of completely rigid fibers, we underline that, under pulsatile flow conditions, that normally appear in large to small vessels, the time-average apparent permeability of the

EGL can be one or two orders of magnitude larger than what Darcy law predicts. This finding gives an alternative perspective to the efficiency of paracellular and transcellular transport processes of biological molecules, plasma ions, and viruses. From a modeling viewpoint, should a macroscopic approach be employed, in which the EGL is treated as a porous medium, both the motion and the deformation of the EG should definitely be accounted for. Moreover, our simulation results reveal that the time-averaged apparent permeability varies as a second-order polynomial function of $1/B_R$ and a rational function of H_K . But, under steady state flow conditions, the apparent permeability of EGL is not affected by H_K variations and can be determined by the analytical approximations for rigid EG fibers [27,28].

ACKNOWLEDGMENTS

This work is part of the Research Project “Multiscale modeling for the autoregulation of Microvessels, CARE,” which was supported by the Hellenic Foundation for Research and Innovation (H.F.R.I.) under the “1st Call for H.F.R.I. Research Projects to support Faculty members and Researchers and the procurement of high-cost research equipment” (Project No. 81105).

APPENDIX A: MESH-CONVERGENCE STUDY

The ALE numerical scheme, along with the discontinuous approximation for the pressure field, is a stable formulation that guarantees the accuracy of all variables, even their gradients at the fluid-solid interface and in the bulk. To investigate the mesh and timestep convergence of our numerical solutions we apply the FE formulation on three different meshes with three different time steps. Although we have conducted studies on the mesh-independence of the numerical solutions for both rheometric protocols, here we present only the convergence of the start-up shear flow for $A_R = 30$, $B_R = 0.33$, and $H_K = 89$. In particular, Table VII summarizes the main characteristics of these meshes. Meshes M2 and M3 are generated by sequentially doubling the elements of M1 in each direction, while the time steps of the simulations associated with M2 and M3 are also sequentially halved. All meshes are uniform in both directions.

Figure 23 depicts our results for the fiber-tip displacement components using M1, M2, and M3. As we can see, the proposed numerical scheme features mesh and timestep independence between M2 and M3. To this end, no remeshing of the computational domain has been performed, and in all cases, in terms of the Netgen parameters, a mesh equivalent to M2 is used.

APPENDIX B: ANALYTICAL SOLUTIONS BASED ON THE LINEAR THEORY FOR BEAM DEFORMATION

A question that typically arises is whether the linear theory for beam deformation [13,101] can be safely applied for predicting the characteristic features of the fiber dynamics, such as the vertical compression $-d_y$ and the horizontal extension d_x of the fiber tip. Based on the Sangani and Acrivos’s expressions [26] in the limit of sparse or dense arrays of fibers and the analytical solutions for the velocity profile of a Newtonian fluid flowing over and through a porous medium in a Couette channel by Martys, Bentz, and Garboczi [102] (see also [79,103]), we derive analytical approximations for

TABLE VII. Main characteristics of the meshes used in start-up shear flow.

Mesh	Min. element size	Max. element size	Total no. elements	Total no. nodes	Time step dt
M1	0.7	1.8	85 668	14 958	0.02
M2	0.4	1.8	171 497	25 297	0.01
M3	0.18	1.8	342 671	65 355	0.005

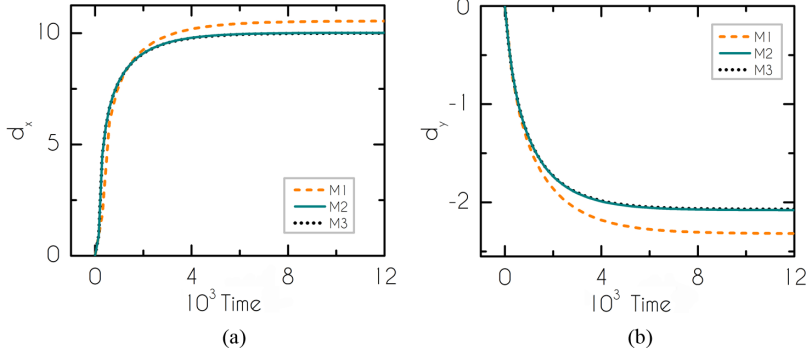


FIG. 23. Fiber-tip displacement components versus time using three different spatial and temporal resolutions. These cases were computed for $A_R = 30$, $B_R = 0.33$, and $H_K = 89$.

the slip length, the ratio of the interfacial to the CFL velocity, and the displacement of the fibers as functions of the vertical direction.

We start with the dimensional form of the Euler-Bernoulli equation for cantilever beams (i.e., the fibers in our case) under steady-state conditions and loading, which depends on the flow conditions via the drag force per unit length (f_d)

$$E_f I_f \frac{d^4 w(y)}{dy^4} = f_d(y), \quad (\text{B1})$$

where

$$f_d(y) = \frac{4\pi}{f_c} \eta_p \tilde{V}(y) \quad (\text{B2})$$

for sparse porous media formed by a hexagonal array of cylinders, f_c , is given by

$$f_c = \ln(c^{-0.5}) - 0.745 + c - \frac{c^2}{4}, \quad \text{with } c \ll 1, \quad (\text{B3})$$

while for dense porous media, f_c obeys the following relationship:

$$f_c = \frac{4\sqrt{2}}{7} \left(1 - \left(\frac{c}{c_m} \right)^{1/2} \right)^{5/2}, \quad c_m = \frac{\pi}{2\sqrt{3}}, \quad \text{with } c - c_m \ll 1, \quad (\text{B4})$$

where c_m is the maximum volume fraction for the hexagonal array and $E_f I_f$ is the flexural rigidity of a fiber, which is the product of the Young modulus E_f and the second moment of area I_f for cylindrical fibers:

$$I_f = \frac{\pi}{4} R_f^4. \quad (\text{B5})$$

$\tilde{V}(y)$ is the velocity distribution in the flow direction within the porous medium (i.e., glycocalyx layer), and according to Martys *et al.* [102] it is given by

$$\tilde{V}(y) = V \exp \left\{ + (y - h_o) \sqrt{\frac{n_p}{n_{pm} K}} \right\}, \quad (\text{B6})$$

where V (or $u_{\text{EGL}}^{\text{max}}$ in dimensionless notation) is the velocity at the interface between the plasma and the porous medium. \tilde{V} corresponds to u_x in the basic control volume presented in Fig. 2.

Furthermore, we assume that the area of the cross section of a fiber is very small compared to the surrounding area, making the effect of the applied force and torque on its tip negligible. At the basis

of the fiber, its slope and its local deflection are zero. These four constraints constitute the boundary conditions for Eq. (B1) [104,105].

The dimensionless slip length is calculated after the assumption that $\tilde{V}(y = h_o - l_{\text{slip}}R_f) = \varepsilon V$, where ε is the zero-velocity threshold and takes values $O(10^{-2})$:

$$l_{\text{slip}} = -\ln(\varepsilon)\sqrt{k_{pm}}, \quad (\text{B7})$$

which agrees with Hosoi's assumption for the thickness of the boundary layer and the extracted Eq. (26).

Solving Eq. (B1) analytically along with its boundary conditions, we determine the variation of the deflection along the y -direction and calculate critical quantities such as the maximum deflection and slope. The local deflection follows

$$\begin{aligned} w(y) = & -\frac{1}{E_f I_f} \frac{4\pi \eta_p V}{\left(\frac{n_p}{n_{pm}K}\right)^2 f_c} \left[\exp\left((y - h_o) \sqrt{\frac{n_p}{n_{pm}K}}\right) - \frac{\left(\frac{n_p}{n_{pm}K}\right)^{\frac{3}{2}}}{6} y^3 \right] \\ & + \frac{1}{E_f I_f} \frac{2\pi \eta_p V}{\left(\frac{n_p}{n_{pm}K}\right) f_c} \left(1 - \sqrt{\frac{n_p}{n_{pm}K}} h_o\right) y^2 + \frac{1}{E_f I_f} \frac{4\pi \eta_p V}{\left(\frac{n_p}{n_{pm}K}\right)^{3/2} f_c} \exp\left(-h_o \sqrt{\frac{n_p}{n_{pm}K}}\right) y \\ & + \frac{1}{E_f I_f} \frac{4\pi \eta_p V}{\left(\frac{n_p}{n_{pm}K}\right)^2 f_c} \exp\left(-h_o \sqrt{\frac{n_p}{n_{pm}K}}\right). \end{aligned} \quad (\text{B8})$$

The dimensionless maximum deflection arises at the fiber tip and in the limit of high enough fibers is given by

$$d_x = \frac{w(h_o)}{R_f} \cong \left[\frac{16}{f_c} V_r \frac{1}{H_K} k_{pm}^2 \left(1 - \frac{1}{6} k_{pm}^{-3/2} A_R^3\right) - \frac{8}{f_c} V_r \frac{1}{H_K} k_{pm} A_R^2 \left(1 - A_R k_{pm}^{-1/2}\right) \right], \quad (\text{B9})$$

while the maximum slope follows is

$$\theta_B = \tan^{-1}(-w'(h_o)) \cong \tan^{-1} \left[\frac{16}{f_c} V_r \frac{1}{H_K} k_{pm}^{\frac{3}{2}} \left(1 - \frac{1}{2} k_{pm}^{-1} A_R^2\right) - \frac{16}{f_c} V_r \frac{1}{H_K} k_{pm} A_R \left(1 - A_R k_{pm}^{-\frac{1}{2}}\right) \right], \quad (\text{B10})$$

where V_r stands for the ratio of the velocity at the plasma/porous medium interface to the CFL velocity

$$V_r = \frac{V}{V_{\text{CFL}}} = \frac{1}{1 + \frac{1}{\sqrt{k_{pm}}} \left(\frac{L}{R_f}\right)}, \quad (\text{B11})$$

and k_{pm} is given by

$$k_{pm} = \frac{f_c}{4c}. \quad (\text{B12})$$

The dimensionalization of the variables is based on the characteristic scales defined in Sec. II.

From the maximum slope, the dimensionless temporal height of a fiber is estimated by the following relationship of Deng *et al.* [88]:

$$h \sim A_R \cos(\theta_B), \quad (\text{B13})$$

while the decrease in height in comparison to its initial value approximately is

$$-d_y \sim A_R [1 - \cos(\theta_B)] \quad (\text{B14})$$

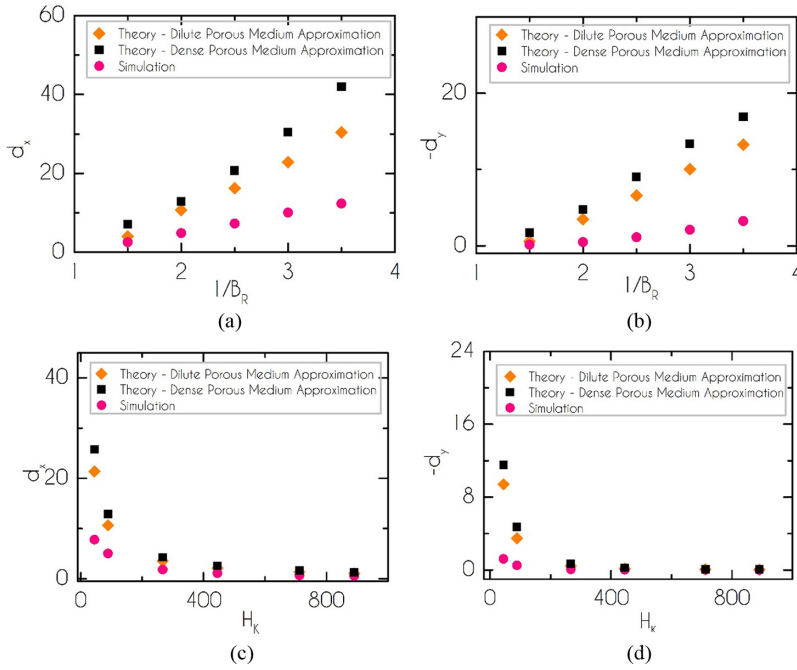


FIG. 24. Variations of the fiber-tip displacement components under steady-state conditions as functions of (a), (b) the inverse of the blockage ratio ($A_R = 30$, $H_K = 89$), and (c), (d) the elasticity number ($A_R = 30$, $B_R = 0.50$). Three methods are used for extracting the results: diamonds correspond to predictions based on the theoretical linear beam deformation theory for dilute porous media [Eq. (B3)], squares are also based on the same theory but in the limit of dense glycocalyx [Eq. (B4)], and circles are outcomes of our simulations.

This is an approximation because the small-deflection theory does not account for the variation in the vertical direction. Of course, there are more realistic 1D models that account for it, such as the large deflection model used by Pozrikidis [104,105] and Wexler *et al.* [106], but they have no closed-form analytical solution and must be solved numerically.

The analytical model presented herein captures the dependence of the fiber-tip displacement component on the blockage ratio (B_R) and the elasticity number (H_K). d_x and d_y vary linearly and quadrately with the inverse of both dimensionless parameters (Fig. 24). There is a distinct deviation between the predictions of our numerical simulations and the solution of the analytical model. Their discrepancy is smaller when the fibers become stiffer or the spacing among them larger because basic features of the model have been derived under such assumptions [Eqs. (B1), (B3), (B6), (B11)]. In all cases, the dense-limit approximation [Eq. (B4)] provides larger predictions than the sparse-limit one [Eq. (B3)], and both systematically overestimate the tip displacement vector for the whole range of our simulations. Both conclusions agree with the range of validity of each analytical formula [26]. Indicatively, the sparse-limit formula is valid for $c < 0.4$ or $B_R < 0.65$. Thus, the answer to the initial question of the appendix is that analytical models can not be safely used for extracting accurate predictions for basic features of the glycocalyx layer. This holds even for the current approximate model, which is more complete than previous ones (see [79,30]) for the flow through an array of flexible fibers. These findings can explain the failure of Weinbaum *et al.* [13] to provide a reliable estimation of the flexural rigidity of fibers using the Euler-Bernoulli model for point loading and experimental data from the recoiling of glycoproteins after the passage of a white blood cell.

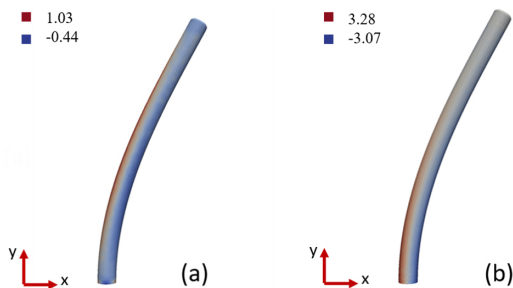


FIG. 25. (a) Shear stress σ_{xy} and (b) normal stress σ_{yy} distribution on an EG fiber. Presented data were computed at steady state for $B_R = 0.33$, $H_K = 89$, and $A_R = 30$.

APPENDIX C: EGL STRUCTURAL STRESSES

The proposed large-scale model provides valuable data for the structural dynamics of the fibers. The stresses resulting from the deformation of the glycoproteins are indicators of their biological and mechanical integrity. Regions with a high accumulation of stresses along the fiber body are locations for initiating a failure. Moreover, any mechanical signal which corresponds to a variation of the structural stresses is transmitted from the fiber body to the endothelium, controlling its dynamical response and homeostasis. A typical example of a cascade of events could be an increase in blood velocity, which causes large deformations of the glycoproteins and signals the increased production of NO, a vasodilator causing the widening of the vessels.

In Fig. 25 we present contours of the shear σ_{xy} and normal σ_{yy} stress on the surface of a fiber at the final sufficiently deformed state for $B_R = 0.33$, $H_K = 89$, and $A_R = 30$. Given that plasma flow and fibers displacement is in the x -direction, in (a) one can see that high positive values of σ_{xy} up to 1.03 appear at the curved part of the fiber elongated by the deformation of the fibers, while high negative values up to 0.44 appear at the shortened curved part. On the other hand, the normal stress is increased at the bottom part of the body of the fiber. Specifically, at the left side of the fiber [Fig. 25(b)], where tension dominates, normal stress reaches values up to 3.28. Accordingly, negative normal stress due to compression is observed at the right side with the highest absolute value of 3.07 at the base of EG. The value of both stress components is zero near the fiber tips in steady state revealing how glycocalyx may feel and translate lateral forces imposed by the plasma flow into concentrated stress close to the endothelial membrane, supporting its role as a transducer of mechanical stress [13–15].

-
- [1] A. R. Pries, T. W. Secomb, and P. Gaehtgens, The endothelial surface layer, *Pflügers Arch.* **440**, 653 (2000).
 - [2] H. Gitay-Goren, S. Soker, I. Vlodaysky, and G. Neufeld, The binding of vascular endothelial growth factor to its receptors is dependent on cell surface-associated heparin-like molecules, *J. Biol. Chem.* **267**, 6093 (1992).
 - [3] M. Rusnati and M. Presta, Interaction of angiogenic basic fibroblast growth factor with endothelial cell heparan sulfate proteoglycans. Biological implications in neovascularization, *Int. J. Clin. Lab. Res.* **26**, 15 (1996).
 - [4] M. J. Mitchel and M. R. King, The role of cell glycocalyx in vascular transport of circulating tumor cells, *Am. J. Physiol. Cell Physiol.* **306**, C89 (2014).
 - [5] H. R. Lijnen and D. Collen, Endothelium in hemostasis and thrombosis, *Prog. Cardiovasc. Dis.* **39**, 343 (1997).
 - [6] B. M. Fu, R. H. Adamson, and F. E. Curry, Test of two-pathway model for small solute exchange across the capillary wall, *Am. J. Physiol.* **274**, H2062 (1998).

- [7] C. R. Benedict, R. Pakala, and J. T. Willerson, Endothelial-dependent procoagulant and anticoagulant mechanisms. Recent advances in understanding, *Tex. Heart Inst. J.* **21**, 86 (1994).
- [8] K. Ley, Molecular mechanisms of leukocyte recruitment in the inflammatory process, *Cardiovasc. Res.* **32**, 733 (1996).
- [9] J. H. Luft, Fine structures of capillary and endocapillary layer as revealed by ruthenium red, *Fed. Proc.* **25**, 1773 (1966).
- [10] E. E. Ebong, F. P. Macaluso, D. C. Spray, and J. M. Tarbell, Imaging the endothelial glycocalyx in vitro by rapid freezing/freeze substitution transmission electron microscopy, *Arterioscler. Thromb. Vasc. Biol.* **31**, 1908 (2011).
- [11] S. Reitsma, D. W. Slaaf, H. Vink, M. A. M. J. van Zandvoort, and M. G. A. oude Egbrink, The endothelial glycocalyx: Composition, functions, and visualization, *Pflügers Arch.* **454**, 345 (2007).
- [12] T. J. Rabelink and D. de Zeeuw, The glycocalyx—Linking albuminuria with renal and cardiovascular disease, *Nat. Rev. Nephrol.* **11**, 667 (2015).
- [13] S. Weinbaum, X. Zhang, Y. Han, H. Vink, and S. C. Cowing, Mechanotransduction and flow across the endothelial glycocalyx, *Proc. Natl. Acad. Sci. USA* **100**, 7988 (2003).
- [14] M. M. Thi, J. M. Tarbell, S. Weinbaum, and D. C. Spray, The role of the glycocalyx in reorganization of the actin cytoskeleton under fluid shear stress: A “bumper-car” model, *Proc. Natl. Acad. Sci. USA* **101**, 16483 (2004).
- [15] J. M. Tarbell and M. Y. Pahakis, Mechanotransduction and the glycocalyx, *JIM* **259**, 339 (2006).
- [16] C. C. Mitchel, Starling: The formulation of his hypothesis of microvascular fluid exchange and its significance after 100 years, *Exp. Physiol.* **82**, 1 (1997).
- [17] S. Weinbaum, 1997 Whitaker Distinguished Lecture: Models to solve mysteries in biomechanics at the cellular level; a new view of fiber matrix layers, *Ann. Biomed. Eng.* **26**, 627 (1998).
- [18] X. Hu, R. H. Adamson, B. Liu, F. E. Curry, and S. Weinbaum, Starling forces that oppose filtration after tissue oncotic pressure is increased, *Am. J. Physiol. Heart Circ. Physiol.* **279**, H1724 (2000).
- [19] R. H. Adamson, J. F. Lenz, Z. Zhang, G. N. Adamson, S. Weinbaum, and F. E. Curry, Oncotic pressures opposing filtration across non-fenestrated rat microvessels, *J. Physiol.* **557**, 889 (2004).
- [20] Ye Zeng, E. E. Ebong, B. M. Fu, and J. M. Tarbell, The structural stability of the endothelial glycocalyx after enzymatic removal of glycosaminoglycans, *PLoS ONE* **7**, e43168 (2012).
- [21] D. Chappell, K. Hofmann-Kiefer, M. Jacob, M. Rehm, J. Briegel, U. Welsch, P. Conzen, and B. F. Becker, TNF-alpha induced shedding of the endothelial glycocalyx is prevented by hydrocortisone and antithrombin, *Basic Res. Cardiol.* **104**, 78 (2009).
- [22] J. M. Squire, M. Chew, G. Nneji, C. Neal, J. Barry, and C. Michel, Quasi-periodic substructure in the microvessel endothelial glycocalyx: A possible explanation for molecular filtering? *J. Struct. Biol.* **136**, 239 (2001).
- [23] S. Weinbaum, J. M. Tarbell, and E. R. Damiano, The structure and function of the endothelial glycocalyx layer, *Annu. Rev. Bio. Eng.* **9**, 121 (2007).
- [24] S. Kuwabara, The forces experienced by randomly distributed parallel circular cylinders or spheres in a viscous flow at small Reynolds numbers, *J. Phys. Soc. Jpn.* **14**, 527 (1958).
- [25] H. Hasimoto, On the periodic fundamental solutions of the Stokes equations and their application to viscous flow past a cubic array of spheres, *J. Fluid Mech.* **5**, 317 (1959).
- [26] A. S. Sangani and A. Acrivos, Slow flow past periodic arrays of cylinders with application to heat transfer, *Int. J. Multiphase Flow* **8**, 343 (1982).
- [27] R.-Y. Tsay and S. Weinbaum, Viscous flow in a channel with periodic cross-bridging fibres: Exact solutions and Brinkman approximation, *J. Fluid Mech.* **226**, 125 (1991).
- [28] J. J. L. Higdon and G. D. Ford, Permeability of three-dimensional models of fibrous porous media, *J. Fluid Mech.* **308**, 341 (1996).
- [29] C. C. Michel and F. E. Curry, Microvascular permeability, *Physiol. Rev.* **79**, 703 (1999).
- [30] P. Guo, A. M. Weinstein, and S. Weinbaum, A hydrodynamic mechanosensory hypothesis for brush border microvilli, *Am. J. Physiol. Renal Physiol.* **279**, F698 (2000).
- [31] M. Sugihara-Seki and B. M. Fu, Blood flow and permeability in microvessels, *Fluid Dyn. Res.* **37**, 82 (2005).

- [32] A. Alexeev, R. Verberg, and A. C. Balazs, Modeling the motion of microcapsules on compliant polymeric surfaces, *Macromolecules* **38**, 10244 (2005).
- [33] T. Stylianopoulos, A. Yeckel, J. J. Derby, X.-J. Luo, M. S. Shephard, E. A. Sander, and V. H. Barocas, Permeability calculations in three-dimensional isotropic and oriented fiber networks, *Phys. Fluids* **20**, 123601 (2008).
- [34] A. Alexeev, J. M. Yeomans, and A. C. Balazs, Designing synthetic, pumping cilia that switch the flow direction in microchannels, *Langmuir* **24**, 12102 (2008).
- [35] A. Gopinath and L. Mahadevan, Elastohydrodynamics of wet bristles, carpets and brushes, *Proc. R. Soc.* **467**, 1665 (2011).
- [36] F. E. Curry and R. H. Adamson, Endothelial glycocalyx: Permeability barrier and mechanosensor, *Ann. Biomed. Eng.* **40**, 828 (2011).
- [37] E. R. Damiano, B. R. Duling, K. Ley, and T. C. Skalak, Axisymmetric pressure-driven flow of rigid pellets through a cylindrical tube lined with a deformable porous wall layer, *J. Fluid Mech.* **314**, 163 (1996).
- [38] H. Vink, B. R. Duling, and J. A. E. Spaan, Mechanical properties of the endothelial surface layer, *FASEB J.* **13**, A11 (1999).
- [39] E. R. Damiano and T. M. Stace, A mechano-electrochemical model of radial deformation of the capillary glycocalyx, *Biophys. J.* **82**, 1153 (2002).
- [40] Y. Han, S. Weinbaum, J. A. E. Spaan, and H. Vink, Large-deformation analysis of the elastic recoil of fibre layers in a Brinkman medium with application to the endothelial glycocalyx, *J. Fluid Mech.* **554**, 217 (2006).
- [41] P. P. Sumets, J. E. Cater, D. S. Long, and R. J. Clarke, A boundary-integral representation for biphasic mixture theory, with application to the post-capillary glycocalyx, *Proc. R. Soc. London A* **471**, 20140955 (2015).
- [42] T. C. Lee, D. S. Long, and R. J. Clarke, Effect of endothelial glycocalyx layer redistribution upon microvessel poroelastohydrodynamics, *J. Fluid Mech.* **798**, 812 (2016).
- [43] P. P. Sumets, J. E. Cater, D. S. Long, and R. J. Clarke, Electro-poroelastohydrodynamics of the endothelial glycocalyx layer, *J. Fluid Mech.* **838**, 284 (2018).
- [44] E. R. Cruz-Chu, A. Malafeev, T. Pajarskas, I. V. Pivkin, and P. Koumoutsakos, Structure and response to flow of the glycocalyx layer, *Biophys. J.* **106**, 232 (2014).
- [45] X. Z. Jiang, H. Gong, K. H. Luo, and Y. Ventikos, Large-scale molecular dynamics simulation of coupled dynamics of flow and glycocalyx: Towards understanding atomic events on an endothelial cell surface, *J. R. Soc., Interface* **14**, 20170780 (2017).
- [46] J. Alvarado, J. Comet, E. de Langre, and A. E. Hosoi, Nonlinear flow response of soft hair beds, *Nat. Phys.* **13**, 1014 (2017).
- [47] O. du Roure, A. Lindner, E. N. Nazockdast, and M. J. Shelley, Dynamics of flexible fibers in viscous flows and fluids, *Annu. Rev. Fluid Mech.* **51**, 539 (2019).
- [48] K. Hood, M. S. Suryateja Jammalamadaka, and A. E. Hosoi, Marine crustaceans with hairy appendages: Role of hydrodynamic boundary layers in sensing and feeding, *Phys. Rev. Fluids* **4**, 114102 (2019).
- [49] M. Ghisalberti, Obstructed shear flows: Similarities across systems and scales, *J. Fluid Mech.* **641**, 51 (2009).
- [50] C. Wong, P. Trinh, and S. Chapman, Shear-induced instabilities of flows through submerged vegetation, *J. Fluid Mech.* **891**, A17 (2020).
- [51] B. Kruijt, Y. Malhi, J. Lloyd, A. D. Nobre, A. C. Miranda, M. G. P. Pereira, A. Culf, and J. Grace, Turbulence statistics above and within two Amazon rain forest canopies, *Boundary-Layer Meteorol.* **94**, 297 (2000).
- [52] P. Jain, G. L. Baker, and M. L. Bruening, Applications of polymer brushes in protein analysis and purification, *Annu. Rev. Anal. Chem.* **2**, 387 (2009).
- [53] E. A. Schwartz, M. L. Leonard, R. Bizios, and S. S. Bowser, Analysis and modeling of the primary cilium bending response to fluid shear, *Am. J. Physiol.* **272**, F132 (1997).
- [54] C. L. Tien and K. Vafai, Convective and radiative heat transfer in porous media, *Adv. Appl. Mech.* **27**, 225 (1990).

- [55] C. Ni, C. Deck, K. S. Vecchio, and P. R. Bandaru, Optical determination of the flexural rigidity of carbon nanotube ensembles, *Appl. Phys. Lett.* **92**, 173106 (2008).
- [56] A. N. Ford and D. V. Papavassiliou, Flow around surface-attached carbon nanotubes, *Ind. Eng. Chem. Res.* **45**, 1797 (2006).
- [57] J. H. Walther, T. Werder, R. L. Jaffe, and P. Koumoutsakos, Hydrodynamic properties of carbon nanotubes, *Phys. Rev. E* **69**, 062201 (2004).
- [58] P. S. Doyle, E. S. G. Shaqfeh, and A. P. Gast, Rheology of “Wet” Polymer Brushes via Brownian Dynamics Simulation: Steady vs Oscillatory Shear, *Phys. Rev. Lett.* **78**, 1182 (1997).
- [59] W. Reinke, P. Gaehtgens, and P. C. Johnson, Blood viscosity in small tubes: Effect of shear rate, aggregation, and sedimentation, *Am. J. Physiol.* **253**, H540 (1987).
- [60] S. Kim, P. Ong, O. Yalcin, M. Intaglietta, and P. Johnson, The cell-free layer in microvascular blood flow, *Biorheology* **46**, 181 (2009).
- [61] M. Brust, C. Schaefer, R. Doerr, L. Pan, M. Garcia, P. E. Arratia, and C. Wagner, Rheology of Human Blood Plasma: Viscoelastic Versus Newtonian Behavior, *Phys. Rev. Lett.* **110**, 078305 (2013).
- [62] S. Varchanis, Y. Dimakopoulos, C. Wagner, and J. Tsamopoulos, How viscoelastic is human blood plasma?, *Soft Matter* **14**, 4238 (2018).
- [63] G. Marsh and R. E. Waugh, Quantifying the mechanical properties of the endothelial glycocalyx with atomic force microscopy, *J. Vis. Exp.* **72**, e50163 (2013).
- [64] O. Stein, T. Chajek, and Y. Stein, Ultrastructural localization of concanavalin A in the perfused rat heart, *Lab. Invest.* **35**, 103 (1976).
- [65] A. Whyte, L. Garrat, P. S. James, and R. M. Binns, Distribution of saccharides in pig lymph-node high-endothelial venules and associated lymphocytes visualized using fluorescent lectins and confocal microscopy, *Histochem. J.* **25**, 726 (1993).
- [66] B. M. Van den Berg, H. Vink, and J. A. E. Spaan, The endothelial glycocalyx protects against myocardial edema, *Circ. Res.* **92**, 592 (2003).
- [67] N. Maeda, Y. Suzuki, J. Tanaka, and N. Tateishi, Erythrocyte flow and elasticity of microvessels evaluated by marginal cell-free layer and flow resistance, *Am. J. Physiol.* **271**, H2454 (1996).
- [68] S. Kim, R. L. Long, A. S. Popel, M. Intaglietta, and P. C. Johnson, Temporal and spatial variations of cell-free layer width in arterioles, *Am. J. Physiol.* **293**, H1526 (2007).
- [69] Y. Dimakopoulos and J. Tsamopoulos, A quasi-elliptic transformation for moving boundary problems with large anisotropic deformations, *J. Comput. Phys.* **192**, 494 (2003).
- [70] N. Chatzidai, A. Giannousakis, Y. Dimakopoulos, and J. Tsamopoulos, On the elliptic mesh generation in domains containing multiple inclusions and undergoing large deformations, *J. Comput. Phys.* **228**, 1980 (2009).
- [71] Y. Dimakopoulos, A. C. B. Bogaerds, P. D. Anderson, M. A. Hulsen, and F. P. T. Baaijens, Direct numerical simulation of a 2D-stented aortic heart valve at physiological flow rates, *Comput. Meth. Biomech. Biomed. Eng.* **15**, 1157 (2012).
- [72] Y. Dimakopoulos, G. Kelesidis, S. Tsouka, G. C. Georgiou, and J. Tsamopoulos, Hemodynamics in stenotic vessels of small diameter under steady state conditions: Effect of viscoelasticity and migration of red blood cells, *Biorheology* **52**, 183 (2015).
- [73] D. Fraggedakis, J. Papaioannou, Y. Dimakopoulos, and J. Tsamopoulos, Discretization of three-dimensional free surface flows and moving boundary problems via elliptic grid methods based on variational principles, *J. Comput. Phys.* **344**, 127 (2017).
- [74] Y. Bazilevs, K. Takizawa, and T. E. Tezduyar, *Computational Fluid–Structure Interaction: Methods and Applications* (Wiley, New York, 2013).
- [75] J. Schöberl, NETGEN: An advancing front 2D/3D-mesh generator based on abstract rules, *Comput. Visual. Sci.* **1**, 41 (1997).
- [76] H. Fischer, I. Polikarpov, and A. F. Craievich, Average protein density is a molecular-weight-dependent function, *Protein Sci.* **13**, 2825 (2009).
- [77] K. Bai and W. Wang, Spatio-temporal development of the endothelial glycocalyx layer and its mechanical property *in vitro*, *J. R. Soc.* **9**, 2290 (2012).

- [78] D. Chappell, M. Jacob, O. Paul, M. Rehm, U. Welsch, M. Stoeckelhuber, and B. F. Becker, The glycocalyx of the human umbilical vein endothelial cell, *Circ. Res.* **104**, 1313 (2009).
- [79] A. E. Hosoi, Corrsin lecture on hairy hydrodynamics, *Phys. Rev. Fluids* **4**, 110508 (2019).
- [80] M. P. Dalwadi, J. R. King, R. J. Dyson, and K. P. Arkill, Mathematical model to determine the effect of a sub-glycocalyx space, *Phys. Rev. Fluids* **5**, 043103 (2020).
- [81] R. B. Bird, R. C. Armstrong, and O. Hassager, *Dynamics of Polymeric Liquids 1: Fluid Mechanics*, 2nd ed. (John Wiley & Sons, New York, 1987).
- [82] D. A. Fedosov, B. Caswell, A. S. Popel, and G. E. Karniadakis, Blood flow and cell-free layer in microvessels, *Microcirculation* **17**, 615 (2010).
- [83] V. Introvini, A. Carciati, G. Tomaiuolo, P. Cicuta, and S. Guido, Endothelial glycocalyx regulates cytoadherence in *Plasmodium falciparum* malaria, *J. R. Soc. Interface* **15**, 149 (2018).
- [84] T. W. Secomb, Blood flow in the microcirculation, *Annu. Rev. Fluid Mech.* **49**, 443 (2017).
- [85] Y. Han, P. Ganatos, and S. Weinbaum, Transmission of steady and oscillatory fluid shear stress across epithelial and endothelial surface structures, *Phys. Fluids* **17**, 031508 (2005).
- [86] See Supplemental Material at <http://link.aps.org/supplemental/10.1103/PhysRevFluids.7.013102> for movies. Movie 1: Response to steady bloodstream along with contour lines of the displacement magnitude on the fiber body for $BR = 3$, $HK = 89$. Blue and red, respectively, represent the min (0) and max values (10.21). For the visualization of the EGL, we have used four consecutive elementary domains in the direction of the symmetry (z-direction), and eight in the direction of periodicity (x-direction). Movie 2: Response to oscillatory bloodstream along with contour lines of the displacement magnitude on the fiber body for $BR = 3$, $HK = 89$. Blue and red, respectively, represent the min (0) and max values (10.21). For the visualization of the EGL, we have used four consecutive elementary domains in the direction of the symmetry (z-direction), and eight in the direction of periodicity (x-direction).
- [87] D. Pettas, G. Karapetsas, Y. Dimakopoulos, and J. Tsamopoulos, On the degree of wetting of a slit by a liquid film flowing along an inclined plane, *J. Fluid Mech.* **820**, 5 (2017).
- [88] M. Deng, X. Li, H. Liang, B. Caswell, and G. E. Karniadakis, Simulation and modelling of slip flow over surfaces grafted with polymer brushes and glycocalyx fibres, *J. Fluid Mech.* **711**, 192 (2012).
- [89] A. M. J. Davis and E. Lauga, Hydrodynamic friction of fakir-like superhydrophobic surfaces, *J. Fluid Mech.* **661**, 402 (2010).
- [90] J. P. Rothstein, Slip on superhydrophobic surfaces, *Annu. Rev. Fluid Mech.* **42**, 89 (2010).
- [91] C. Ybert, C. Barentin, C. Cottin-Bizonne, P. Joseph, and L. Bocquet, Achieving large slip with superhydrophobic surfaces: Scaling laws for generic geometries, *Phys. Fluids* **19**, 123601 (2007).
- [92] Y. Peng, C. M. Serfass, C. N. Hill, and L. C. Hsiao, Bending of soft micropatterns in elastohydrodynamic lubrication tribology, *Exp. Mech.* **61**, 969 (2021).
- [93] Y. C. Fung, in *Biomechanics: Circulation*, 2nd ed. (Springer-Verlag, New York, 1997), p. 978.
- [94] V. Fuster, R. Harrington, J. Narula, and Z. Eapen, in *Hurst's The Heart*, 14th ed. (McGraw-Hill Education/Medical, New York, 2017), p. 235.
- [95] K. Giannokostas, D. Pothinos, Y. Dimakopoulos, and J. Tsamopoulos, Quantifying the non-Newtonian effects of pulsatile hemodynamics in tubes, *J. Non-Newtonian Fluid Mech.* **298**, 104673 (2021).
- [96] S. Varchanis, G. Makrigrigios, P. Moschopoulos, Y. Dimakopoulos, and J. Tsamopoulos, Modeling the rheology of thixotropic elasto-visco-plastic materials, *J. Rheol.* **63**, 609 (2019).
- [97] K. Giannokostas, Y. Dimakopoulos, A. Anayiotos, and J. Tsamopoulos, Advanced constitutive modeling of the thixotropic elasto-visco-plastic behavior of blood: Steady state blood flow in microtubes, *Materials* **14**, 367 (2021).
- [98] K. Giannokostas, P. Moschopoulos, S. Varchanis, Y. Dimakopoulos, and J. Tsamopoulos, Advanced constitutive modeling of the thixotropic elasto-visco-plastic behavior of blood: Description of the model and rheological predictions, *Materials* **13**, 4184 (2020).
- [99] T. W. Secomb, R. Hsu, and A. R. Pries, A model for red blood cell motion in glycocalyx-lined capillaries, *Am. J. Physiol.* **274**, H1016 (1998).
- [100] T. W. Secomb, R. Hsu, and A. R. Pries, Effect of the endothelial surface layer on transmission of fluid shear stress to endothelial cells, *Biorheology* **38**, 143 (2001).

- [101] J. M. Gere and B. J. Goodno, *Mechanics of Materials*, 8th ed. (Cengage Learning, Stanford, USA, 2012).
- [102] N. Martys, D. P. Bentz, and E. J. Garboczi, Computer simulation study of the effective viscosity in Brinkman's equation, *Phys. Fluids* **6**, 1434 (1994).
- [103] T. S. Alexiou and G. E. Kapellos, Plane Couette-Poiseuille flow past a homogeneous poroelastic layer, *Phys. Fluids* **25**, 073605 (2013).
- [104] C. Pozrikidis, Shear flow over cylindrical rods attached to a substrate, *J. Fluids Struct.* **26**, 393 (2010).
- [105] C. Pozrikidis, Shear flow past slender elastic rods attached to a plane, *Int. J. Solids Struct.* **48**, 137 (2011).
- [106] J. S. Wexler, P. H. Trinh, H. Berthet, N. Quennouz, O. du Roure, H. E. Huppert, A. Lindner, and H. A. Stone, Bending of elastic fibres in viscous flows: The influence of confinement, *J. Fluid Mech.* **720**, 517 (2013).